



Advanced Test Equipment Rentals

www.atecorp.com 800-404-ATEC (2832)

The objective of this study was to determine the appropriate and most accurate use of B-dot and D-dot probes when used to measure the electromagnetic (EM) field inside a cavity. The purpose of this study was to investigate the measurement accuracy of the probes as a function of three different configurations (detailed later) and to determine which probe was more suitable for a given configuration. This study also investigated the effects of coupling between identical probes when used in close proximity to each other. The main result of this study was the determination of how each probe reacted to the various configurations in the far field. The far field was used because E-incident and H-incident field intensities could easily be calculated. These calculated values were then compared to the measured values of the detected voltage response of the probe in an anechoic chamber.

The specific purpose of this study is to develop several new measurement techniques which could be used to test actual Air Force system equipment and to measure electromagnetic field intensities and mode configurations inside partially shielded cavities.

II. TEST SETUP

The following equipment was used in the anechoic chamber tests:

A. Equipment Used

HP8350B	University of Colorado	Anechoic Chamber
HP83592A	Hewlett Packard	Sweep Oscillator
HP432A	Hewlett Packard	RF Plug-In
HP478A	Hewlett Packard	Power Meter
27000	Narda	Thermistor Mount (200 ohm)
		50dB High Power
		Directional Coupler
HP70000 series	Hewlett Packard	Spectrum Analyzer
HP70906A	Hewlett Packard	RF Section
HP70902A	Hewlett Packard	IF Section
HP70900A	Hewlett Packard	LO Section
RGA-180	Electrometrics	Horn
JR630-200	Keltec	TWT Amplifier 8.5-17.0GHz
XR630-200	Keltec	TWT Amplifier 4.0-8.0GHz
SR630-200	Keltec	TWT Amplifier 2.0-4.0 GHz
LR630-200	Keltec	TWT Amplifier 1.0-2.0GHz
CM702	AGA	Thermovision Color Monitor
780	AGA	Thermovision Display Unit
2A	AGA	Oscar
722	Amdek	Color Monitor
290	Midwest Microwave	30dB Feedthru
	IBM	AT Personal Computer
	AGA	Thermovision IR Camera
	Quickset	Tripod
	University of Colorado	Wood Frame

B. Test Setup

Probe measurements were made in the Anechoic Chamber at the University of Colorado. A sweep oscillator was used to provide the initial RF power feeding one of the TWT amplifiers through an SMA cable. The output of the amplifier was fed to the input of a 50dB directional coupler. The directional coupler was connected through an access panel of the Anechoic chamber to a power cable providing RF power to the horn. The input power to the horn was monitored by placing one end of a 200 ohm thermistor mount on the incident port of the directional coupler and recording the incident power with a power meter.

The probes were set up in a manner to allow for total suspension in the air without obstacles blocking or interfering with the measurements. This was accomplished by constructing a 3' X 3' wood frame comprised of 2" X 4" 's and placing the probe in the center of the structure. Absorbent material was also placed in front of the wood to prevent further reflections. Low dielectric line was used to position the probe within the wooden frame in several different configurations. The power received by the probe was monitored on a SMA cable coupled through the chamber wall to a Spectrum Analyzer. The equipment set up is shown in Figure 1a. The test set up is shown in Figure 1b.

C. Probes

This study dealt with two different probes, one was a D-dot probe and the other was a B-dot probe. Schematic diagrams of the D-dot and B-dot probes tested in the anechoic chamber are shown in Figure 2. Figure 2 also shows the assignment of the port labels. The B-dot probes were constructed from half loop antennas. These loop antennas measure the component of the magnetic flux density normal to the plane of the loop. The D-dot probes were constructed from monopole antennas over a ground plane. These monopoles measure the component of the electric field intensity tangent to the axis of the monopole.

D. Test Configurations

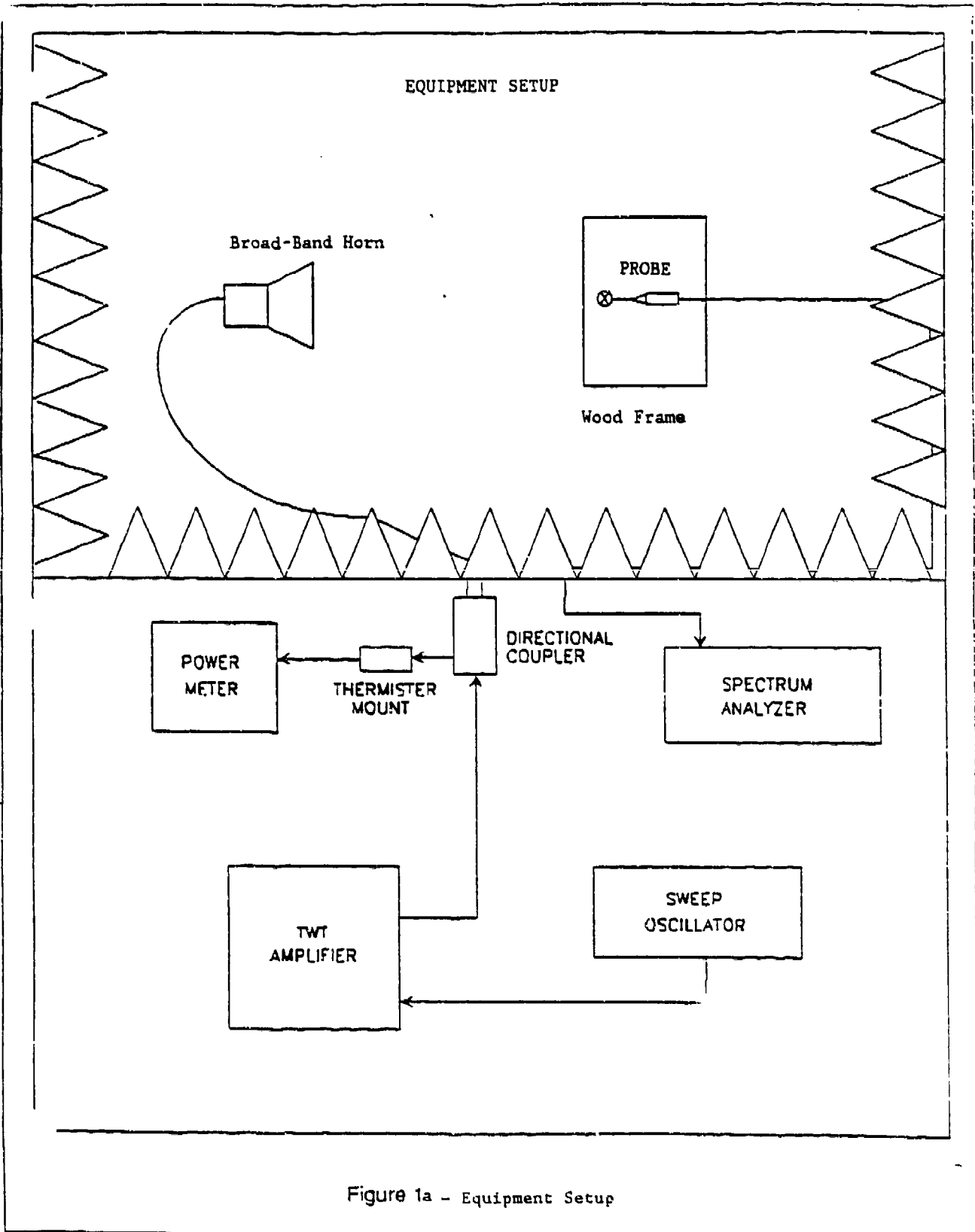
Two different test setup configurations were used. In the first configuration, a single B-dot probe was suspended in free space and illuminated in the frequency range of 1 to 10 GHz. The scattered fields were determined as a function of frequency. In the second configuration, two B-dot probes, at various separations, were also illuminated from 1 to 10 GHz. The coupled fields (including the mutual interaction between the probes) were measured as a function of separation distance and frequency. In all cases, the incident plane wave was vertically polarized.

1. Single Probe Configurations

The probes were used to measure power in three different configurations, as shown in Figure 3.

In configuration A, the axis of the probe is parallel to the direction of propagation of the incident plane wave. The base of the probe is away from the horn.

In configurations B and C, the axis of the probe is perpendicular to the direction of propagation of the incident plane wave. In configuration B, the probe is horizontal, i.e. aligned perpendicular to the direction of polarization; in configuration C, the probe is vertical, i.e. aligned parallel to the direction of polarization.



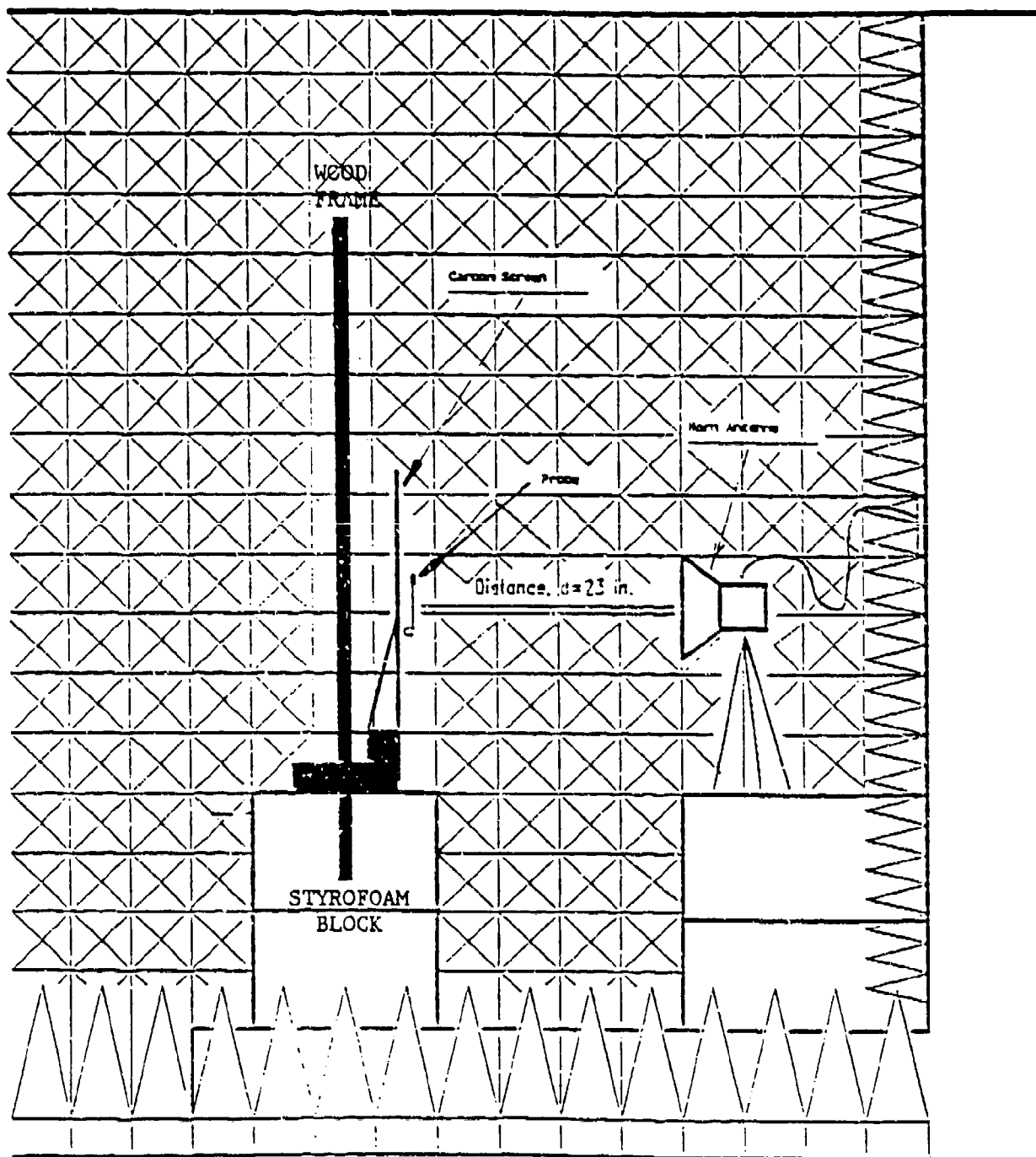


Figure 1b - Test Setup

PROBE OUTPUT PORT IDENTIFICATION

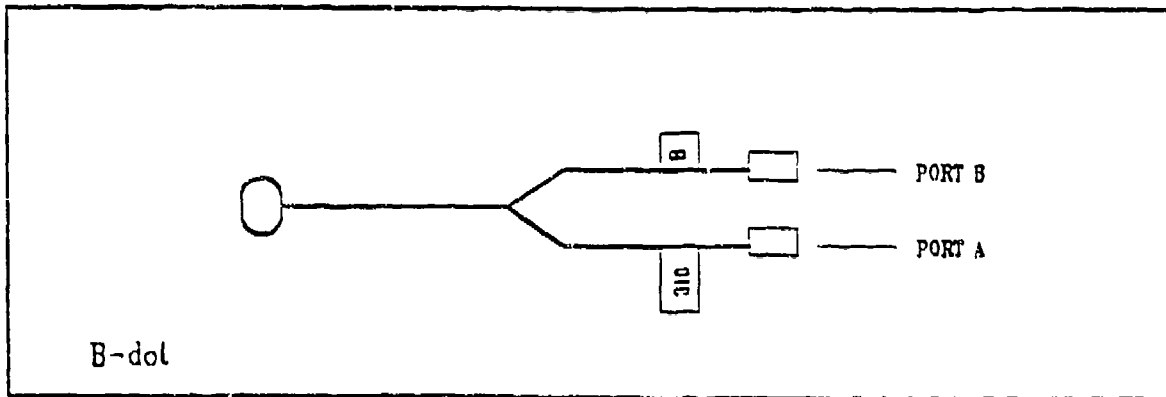
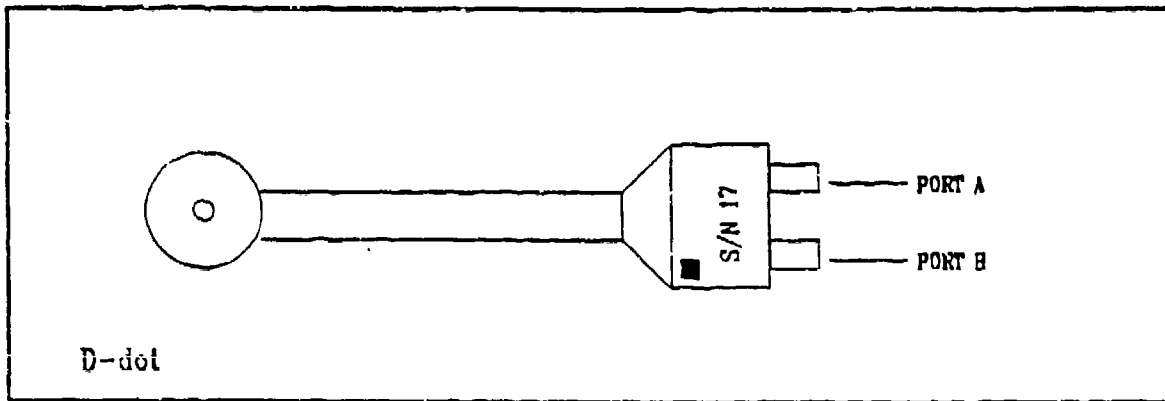


Figure 2 - Probes

PROBE CONFIGURATIONS

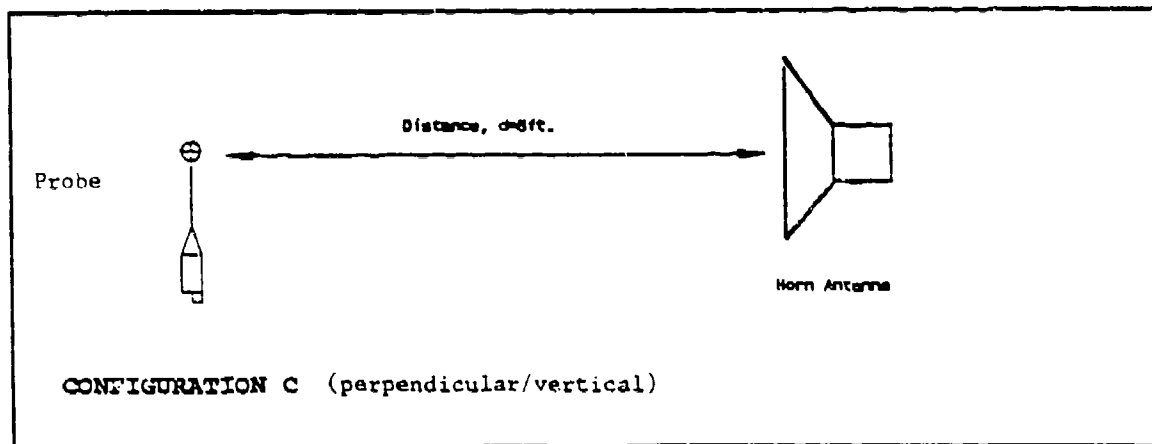
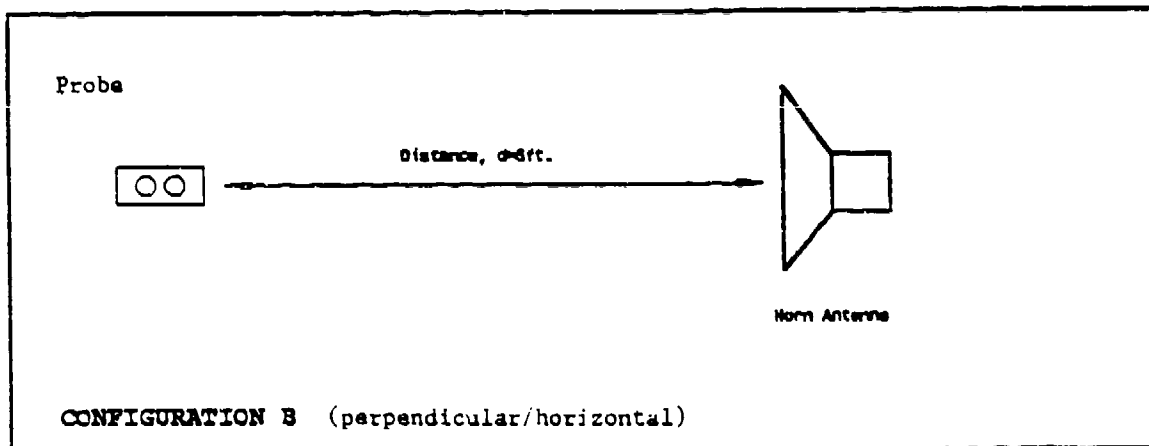
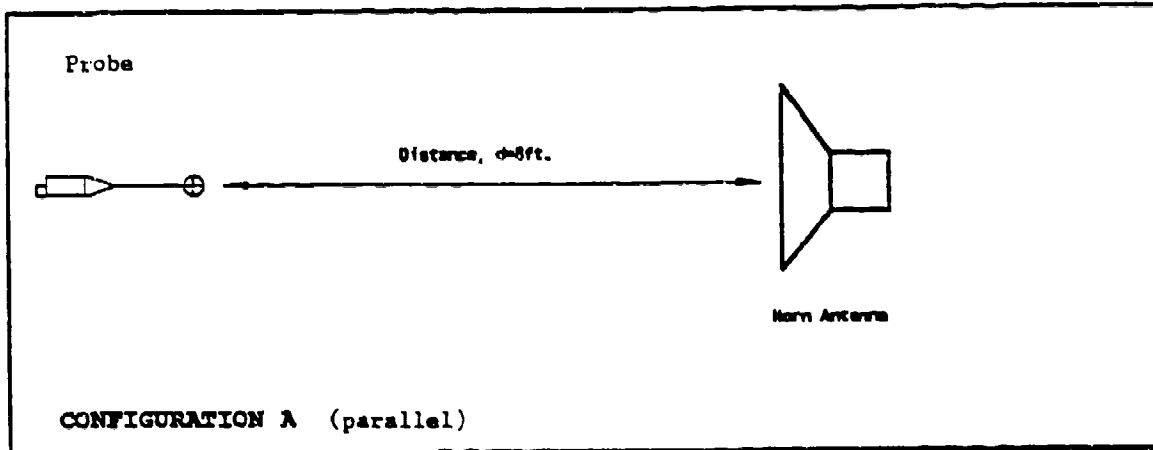
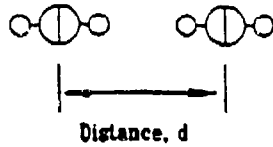


Figure 3 - Probe Configurations

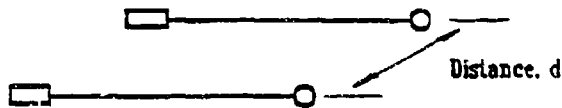
Probe Configurations

Distance, d was varied from 1 cm to 10 cm



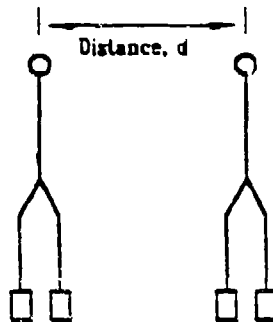
CONFIGURATION A: Horn View

Distance, d was varied from 1 cm to 10 cm



CONFIGURATION B: Horn View

Distance, d was varied from 1 cm to 10 cm



CONFIGURATION C: Horn View

Figure 4 - Probe Configurations

2. Two Probe Configurations

When two probes were used simultaneously, the axes of the two probes were parallel to each other and oriented in configurations A, B and C, also shown in Figure 4. The distance between the probes was varied to determine the effects of mutual coupling and interference between the probes.

III. CALIBRATION

All connecting cables were calibrated using an HP 8510 Network Analyzer. The cable calibration constants determined the power loss through the cables at selected frequencies. The cable calibration results showed a modest increase in power loss as the frequency increased. This is due primarily to cable resistance which is frequency dependent; therefore, the resistance increased as the frequency increased. The power cable calibration constant was measured to obtain an accurate indication of the incident power level being supplied from the horn to the probe. The SMA cable calibration constants were measured so that accurate calculations could be made for the power received by the probe. The cable calibration constants were provided in a table and were used to calculate the incident E and H fields.

IV. PROBE RESPONSE IN THE FREE FIELD

A. Methodology

1. Incident Field Prediction

The Friis Transmission Formula was used to determine incident E and H fields on the probe. The Friis Transmission Formula and an alternative formula are

$$\frac{P_r}{P_t} = \frac{A_t A_r}{d^2 \lambda^2}$$

or

$$\frac{P_r}{P_t} = \frac{G_t A_r}{4 \pi d^2}$$

where

$$G_t = 4\pi \frac{A_t}{\lambda^2}$$

and

P_r = power received by the probe (Watts)

- P_t = power transmitted by the horn (Watts)
 (cable loss not included in this measurement)
 G_t = gain of the horn
 A_r = the effective area of the sensor of the probe (square meters)
 A_t = the effective area of the transmitting horn (square meters)
 d = separation between the horn and probe (meters)
 $\langle S_i \rangle$ = average power density (Watts/square meters)
 S_i = power density (Watts/square meters)
 Z_0 = intrinsic impedance of air
 E_i = E-field incident (Volts/meter)
 H_i = H-field incident (Amps/meter)
 λ = wavelength of incident plane wave

The incident power density in the probe is

$$S_i = \langle S_i \rangle G_t$$

where

$$\langle S_i \rangle = \frac{P_t}{4 \pi d^2}$$

For a plane wave, the incident power density is also related to the incident E and H fields by

$$S_i = \frac{1}{2} \frac{|E_i|^2}{Z_0} = \frac{1}{2} Z_0 |H_i|^2$$

where Z_0 is the impedance of free space

$$Z_0 = \sqrt{\frac{\mu_0}{\epsilon_0}} \approx 377 \Omega$$

The above equations can be combined to give

$$|E_i| = \sqrt{2 Z_0 \frac{P_t G_t}{4 \pi d^2}}$$

and

$$|H_i| = \sqrt{\frac{2}{Z_0} \frac{P_t G_t}{4 \pi d^2}}$$

In free space,

$$|D_i| = \epsilon_0 |E_i| = \epsilon_0 \sqrt{2Z_0 \frac{P_t G_t}{4\pi d^2}}$$

$$|B_i| = \mu_0 |H_i| = \mu_0 \sqrt{2 \frac{P_t G_t}{Z_0 4\pi d^2}}$$

2. Incident Field Measurement

The B-dot and D-dot probes measure the incident B and D fields, respectively.

For the B-dot probe, the detected output voltage V_B is proportional to the incident B field and is given by

$$V_B = -j\omega B_i A_B$$

where A_B is the effective area of the B-dot probe.

Rearranging yields

$$B_i = -\frac{V_B}{j\omega A_B}$$

Similarly, for the D-dot probe, the detected output voltage V_D is proportional to the incident D field and is given by

$$V_D = -j\omega D_i A_D$$

where A_D is the effective area of the D-dot probe.

Again, rearranging yields

$$D_i = -\frac{V_D}{j\omega A_D}$$

B. Comparison of Probe Responses

In the experiments to follow, the theoretically predicted incident B or D field, as derived from the Friis Transmission Formula, was compared to the experimentally measured incident B or D field, as determined from the B-dot and D-dot probes.

The above equations are reduced to logarithmic form (in dB) and corrected for cable losses. The corrected data are presented in Volume II.

1. Single Probe Configurations

a. Configuration A

i. B-dot Probe

Configuration A (shown in Figure 5) is the ideal configuration for B-dot probe performance. In this configuration, the probe was placed in such a manner that the sensor portion of the probe received virtually no interference from the rest of the probe body or from the cable monitoring the power received. The B-dot probe is essentially a single magnetic dipole loop antenna. When the probe is positioned in such a way that the H-field from the horn is parallel to the axis of the cylindrical pickup loop, the magnetic flux linking in the cylinder will induce a current in the probe. Configuration A with the probe rotated at 90° and 270° will provide the best performance because the H-field is parallel to the axis of the cylinder. Configuration A with 0° or 180° rotation will provide low power readings because the H-field is perpendicular to the axis.

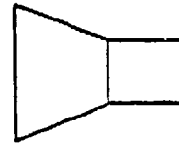
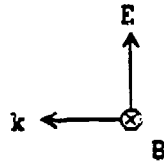
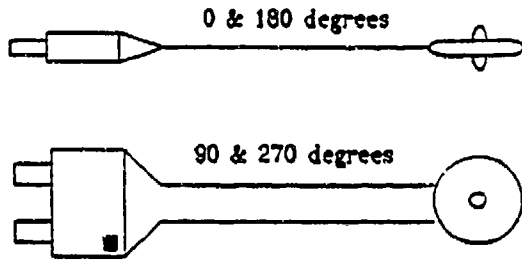
Theoretically, the 90° and 270° rotation measurements should be identical to each other and the 0° and the 180° rotations should be much lower than the measured value at 90° or 270°. Also, it should be immaterial which port is connected to the power meter because each port should function in the same capacity.

Actual measured data on a B-dot probe in configurations A, B and C and in rotations 0°, 90°, 180° and 270° are contained in Volume II, in the section labeled "Single Probe Electrical Measurements." Plots of these data are contained in Volume II, in the section labeled "Single Probe Response Plots."

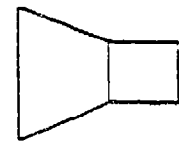
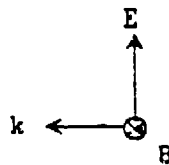
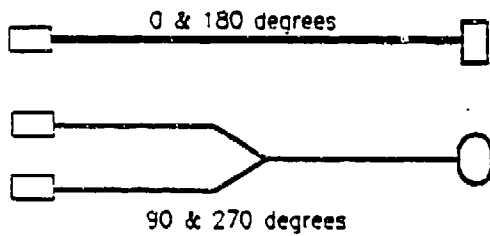
ii. D-Dot Probe

Configuration A is also the ideal configuration for the D-dot probe performance. In this configuration, the probe was placed in a manner such that the sensor portion of the probe received virtually no interference from the rest of the probe body or from the cable monitoring the power received. The D-dot probe is essentially an electric dipole antenna. When the E-field is parallel to the dipole, a current will be induced in the probe. Configuration A with the probe rotated at 0° and 180° provides the best performance because the E-field is parallel to the dipole. Configuration A at 90° and 270° will produce low power readings because the E-field is perpendicular to the dipole.

PROBE ROTATIONS



D-dot



B-dot

Figure 5 - Configuration A

Theoretically, the 0° and 180° rotation measurements should be identical to each other and the 90° and the 270° rotations should be much lower than the measured value at 0° or 180° . It should be immaterial which port is connected to the power meter because each port should function in the same capacity.

Actual measured data on a D-dot probe in configurations A, B and C and in rotations 0° , 90° , 180° and 270° are contained in Volume II, in the section labeled "Single Probe Electrical Measurements." Plots of these data are contained in Volume II, in the section labeled "Single Probe Response Plots."

b. Configuration B

i. B-Dot Probe

Configuration B (shown in Figure 6) is the least favorable of the three configurations for the B-dot probe because regardless of the four different rotations of the probe, 0° , 90° , 180° and 270° , all result in the H-field from the horn being perpendicular to the axis of the cylindrical portion of the sensor. Theoretically, the power measured should be very low.

ii. D-Dot Probe

Configuration B did allow for D-field measurements to be taken by the D-dot probe. This configuration was not as ideal as configuration A because approximately 3 cm of the SMA cable and approximately 1.0 cm of the body of the probe were visible to the incident field from the horn. The resulting reflections produced a destructive interference that degraded the measured power.

c. Configuration C

i. B-Dot Probe

Configuration C (shown in Figure 7) did allow for B-field measurements to be taken by the B-dot probe. This configuration was not as ideal as configuration A because approximately 3 cm of the SMA cable and approximately 1.0 cm of the body of the probe were visible to the incident power from the horn. Since the body of the probe acted as a dipole antenna, a destructive interference, that degraded the measured power, was produced.

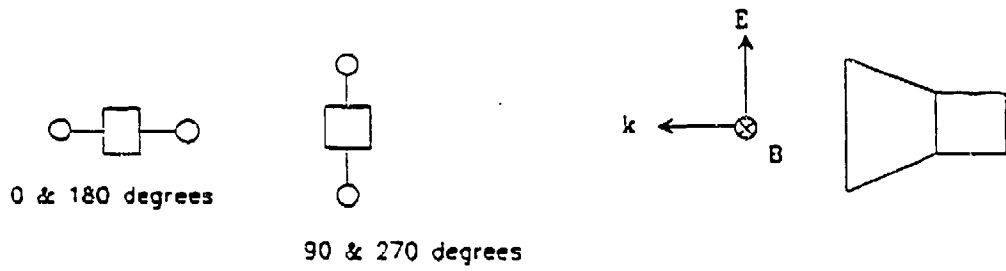
ii. D-Dot Probe

Configuration C is the least favorable of the three configurations for the D-dot probe because, regardless of the four different rotations of the probe, 0° , 90° , 180° and 270° , all result in the E-field from the horn being perpendicular to the axis of the cylindrical portion of the sensor. Theoretically, the power measured should be very low.

PROBE ROTATIONS



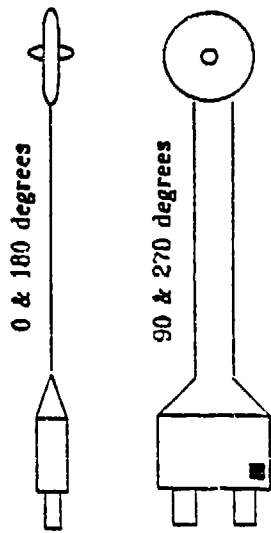
D-dot



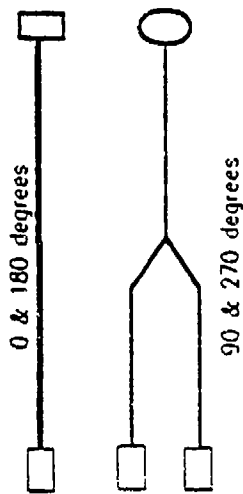
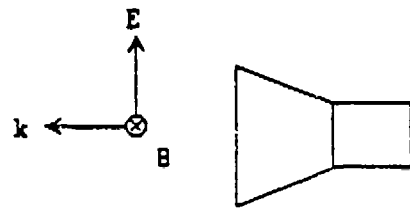
B-dot

Figure 6 - Configuration B

PROBE ROTATIONS



D-dot



B-dot

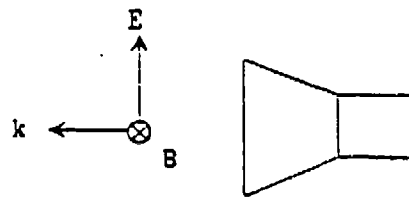


Figure 7 - Configuration C

2. Two-Probe Configurations

To determine the mutual coupling effects between two B-dot and D-dot probes in close proximity, two like probes were placed in the immediate vicinity of each other. One probe (a measurement probe) was connected to the measurement equipment to monitor the incident power levels. The other probe (a dummy probe) was left unconnected but was placed close to the measurement probe to determine the effects of its presence on the measured power level.

As the dummy probe was moved closer to the measurement probe, the measured power level would change due to the interfering effects of the electric or magnetic field reflected from the dummy probe with the incident field being measured by the measurement probe. When the two probes were within one-half wave length of each other, the interference effects were destructive in nature, causing a reduction in the measured power levels. This destructive interference effect is a direct result of the boundary condition on the electric field intensity on the surface of the dummy probe, which requires that the total tangential electric field intensity on the metallic surface of the dummy probe be zero. This results in a 180° phase shift on the metallic surface of the dummy probe, as the incident wave is reflected off the surface of the probe, e.g., the reflected wave, at the surface of the probe, is 180° out of phase with the incident wave.

A small change in separation distance, therefore, will greatly change the power readings when the probes are close together.

Measured data on the B-dot and D-dot probes are contained in Volume II, in the section labeled "Double Probe Electrical Measurements." Relief maps of these data versus frequency and separation distance are shown in Volume II, in the section labeled "Double Probe Response Plots."

C. IR MEASUREMENTS IN THE FREE FIELD

Infrared (IR) pictures of the probe fields were measured to determine the two-dimensional field distribution around the probes. The IR pictures obtained were used to determine how much interference was created between the probes for the various configurations described above.

1. The Infrared Measurement Technique

The investigation of the interaction of the probes with EM waves was undertaken with an Infrared (IR) measurement technique [1-8]. With this IR technique, the two-dimensional field pattern scattered by the probes could be measured in a minimally perturbing way. The interference pattern between two probes could also be measured without introducing another metallic probe in the measurement volume.

The IR technique is based on the Joule heating that occurs in a lossy material as an EM wave passes through the material. The material is assumed to have a finite conductivity, an imaginary permittivity, and an imaginary permeability. The absorbed heat energy is converted into conducted and convected heat energy and into re-radiated electromagnetic energy. This electromagnetic energy is concentrated in the IR band, and can be detected as the energy radiated from a "blackbody" radiator.

The technique involves placing a thin lossy planar detector screen in the vicinity of the probe. The conductivity and the imaginary components of the permittivity and the permeability of the detector material cause the temperature of the detector material to rise above the local ambient temperature of the surrounding environment, by an amount that is proportional to the local electrical and/or magnetic field intensity at each point on the detector screen. This produces a two-dimensional thermal map of the electric and/or magnetic field in the screen material. The thermal distribution is scanned with an IR camera.

The screen material is tailored to be sensitive to only one component of the field. Care is also exercised not to significantly perturb the existing field by the presence of a lossy material. The thickness of the screen material is usually less than 80 microns; the conductivity of the screen material is usually less than 8 mhos per meter.

The temperature difference between the detector material and the background is detected, digitized, and stored in the memory of an AGA Thermo Vision system on a pixel by pixel basis. This stored data represents the temperature distribution over the extent of the detector screen and is a map of the intensity of the electric and/or magnetic field distribution absorbed in the screen. This data was analyzed to determine the interaction of the probe with the incident EM field.

2. IR Results

The first step was to examine the IR pictures when neither probe was present. This would set up a background ambient temperature reference to be used as a comparison for when a probe was present.

The IR pictures were taken from two different positions. One position was with the carbon screen directly behind the probe (axial screen) as shown in Figure 8a. As seen in that figure, the camera is located at approximately 25° to the left of the horn. The other position was with the carbon screen placed transverse to the probe as shown in Figure 8b. As seen in that figure, the IR camera is located at a 90° angle from the horn.

Looking at the axial screen IR pictures it can be seen that configuration A, using either the B-dot or D-dot probe, created the least interference.

As expected, interference from the probes was noticed when IR pictures were taken of configurations B and C. Since the physical size of the D-dot probe is larger than that of the B-dot probe, the interference created by the close proximity of the D-dot probes was greater.

IR data taken in the axial and transverse screens are shown in Volume II, in the section labeled "Free-Field IR Measurements." Figures 9a, b and c contain IR distributions of the interaction of two B-dot probes at 1GHz for 1cm, 5cm and 10cm separation distances, respectively.

V. PROBE RESPONSE IN A CAVITY (CUBE)

A. Methodology

Both the D-dot and B-dot probes were tested inside a cavity to determine probe responses when the probes were used in close proximity in an enclosed area surrounded by metal. A metal cube, one foot on a side was used as a general model for a cavity (hereafter

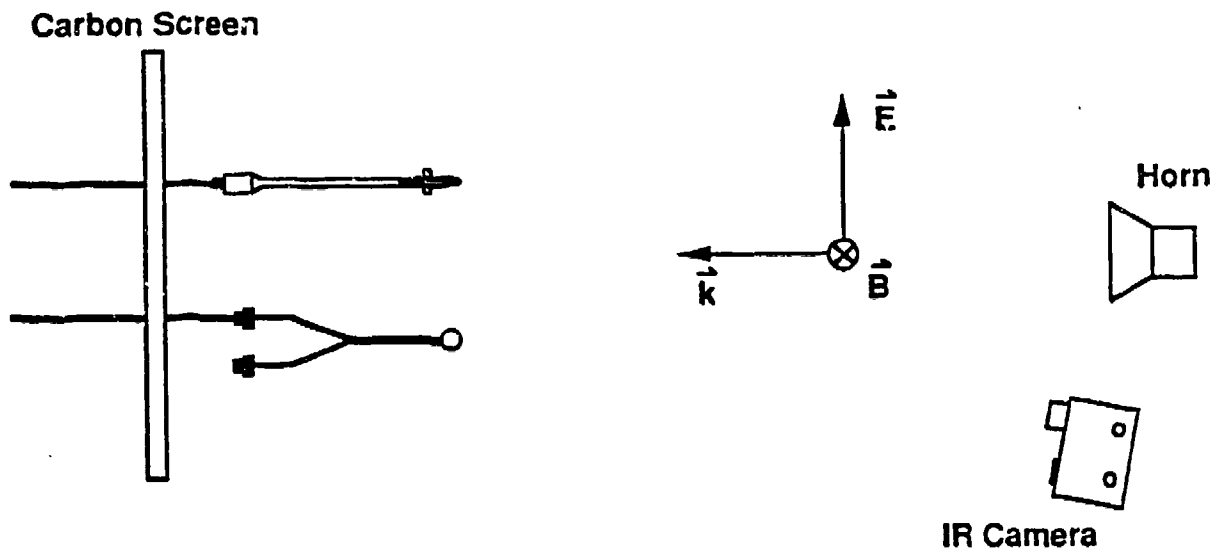


Figure 8a IR Test Set-up (Axial Screen)

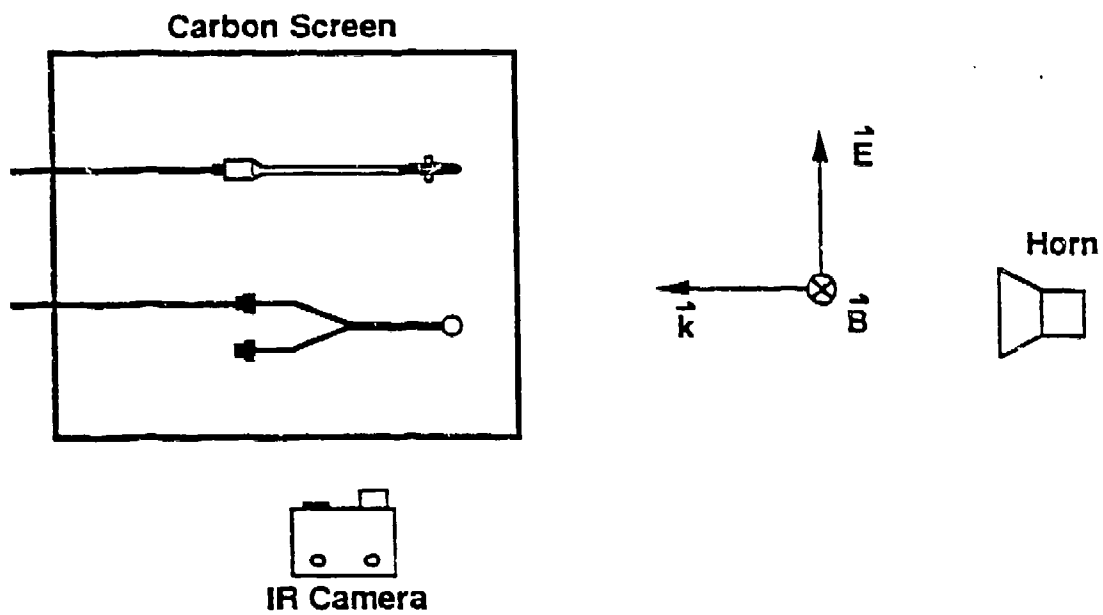


Figure 8b- IR Test Set-up (Transverse Screen)

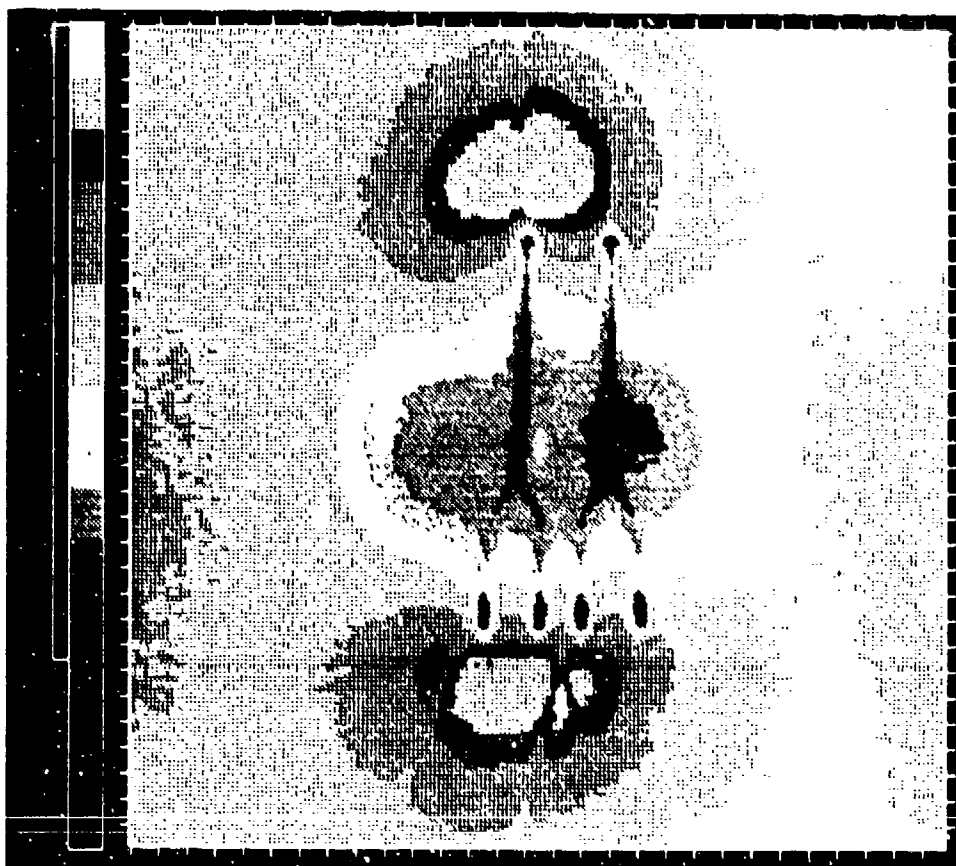


Figure 9a: Two B-dot Probes

1 GHz

1 cm separation

Configuration C - Transverse view

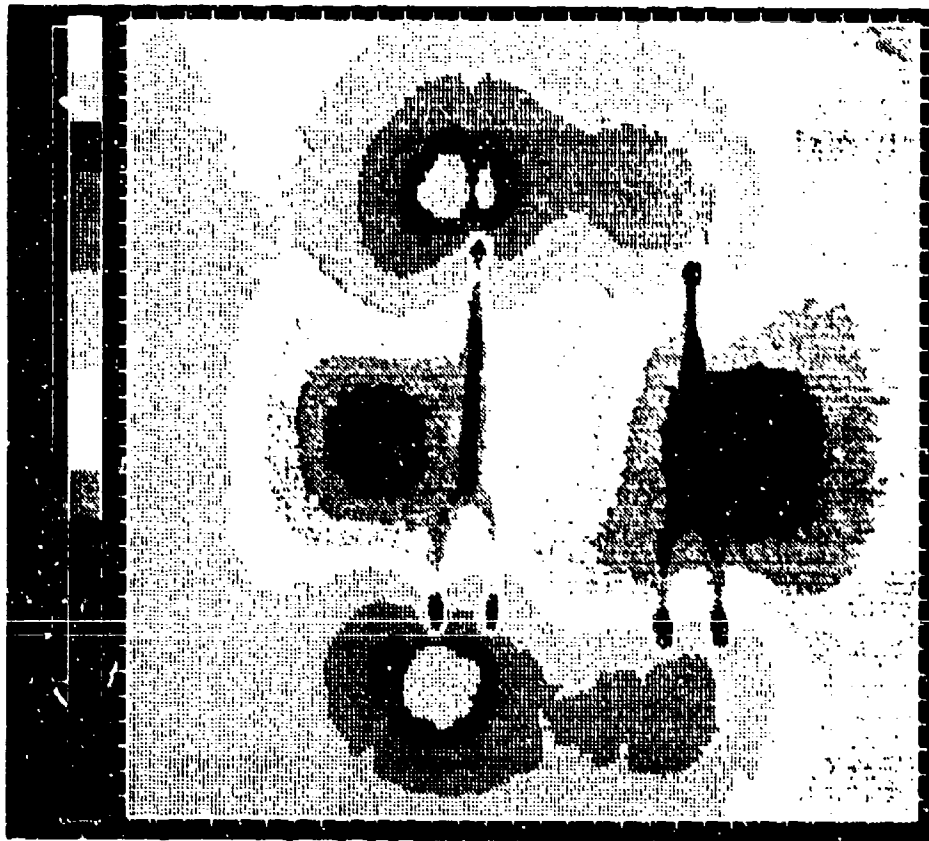


Figure 9b: Two B-dot Probes

1 GHz

5 cm separation

Configuration C - Transverse view

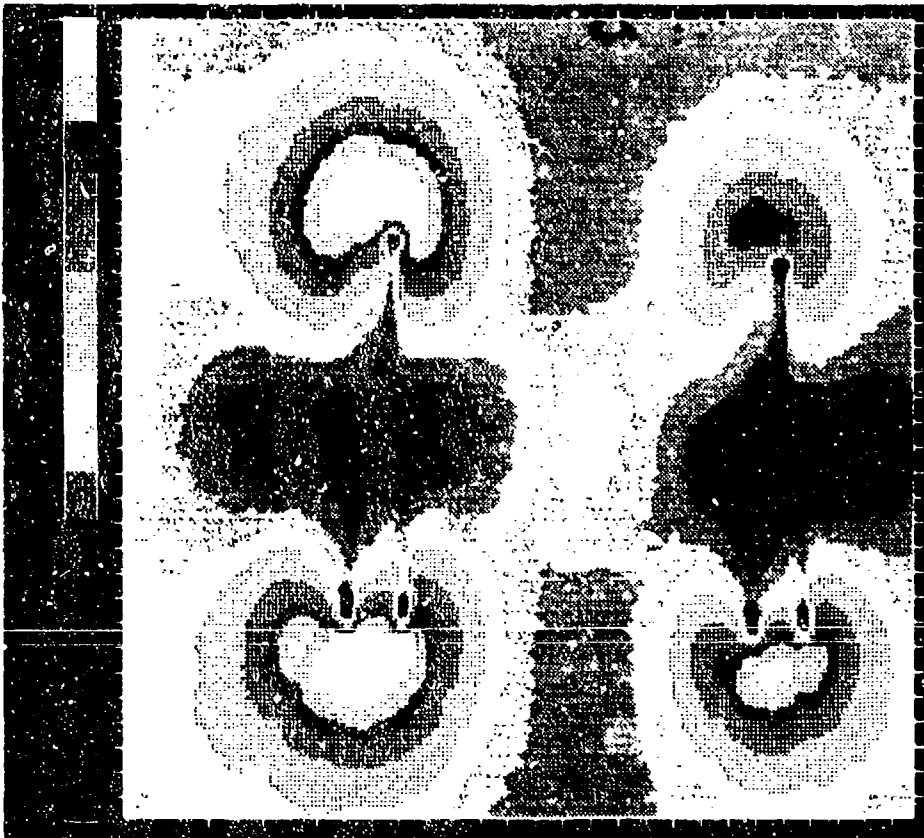


Figure 9c: Two B-dot Probes

1 GHz
10 cm separation

Configuration C - Transverse view

and throughout the report, the cavity will be referred to as the CUBE). A 3" X 1/8" aperture was cut horizontally into the center of one side of the CUBE. On a side directly adjacent to the aperture, a fine wire mesh was used for the wall so that the interior modes of the CUBE could be seen with the IR camera. The CUBE test setup is shown in Figure 10.

The aperture was illuminated with an incident EM wave. The aperture in turn, excited the interior resonant modes of the CUBE. Mathematically, the interior modes are a specific field distribution at a particular frequency that can be described by a summation (Fourier series) of sines, cosines, hyperbolic sines, and hyperbolic cosines. At different frequencies the field distributions will change. A cross section of these field distributions can easily be seen using the IR camera. Electrical measurements and IR pictures of the probes in the CUBE were made. The corrected data are presented in Volume II.

These IR pictures and electrical measurements show that the probe responses are dependent on the particular modes of the CUBE.

B. Electrical Measurements in the CUBE

In the single probe tests, both the D-dot and B-dot probes were used, in all three configurations, at frequencies ranging from 1 to 10 GHz. The measured data show that in the CUBE, the probe response is not as dependent on configuration as in free space. This is because the polarization (direction) of the E and H fields in the CUBE is varying at different points in the CUBE. Here, the E and H fields are incident on the probe from all directions with different orientations. The probe position is important because, for a given mode, the field density is different at different locations in the CUBE. Measured data on the single probe in the CUBE are contained in Volume II, in the section labeled "Single Probe Electrical Measurements in CUBE." Plots of the single probe data are contained in Volume II, in the section labeled "Single Probe Response Plots in CUBE."

In the double probe tests, the D-dot and B-dot probes were used, in all three configurations, at frequencies ranging from 1 to 10 GHz, and at separation distances of 1 to 5 cm. The probe being measured was positioned in the center of the CUBE and a dummy probe was moved away from the center of the CUBE. Measured data on the double probes in the CUBE are contained in Volume II, in the section labeled "Double Probe Electrical Measurements in CUBE." Plots of the double probe data are contained in Volume II, in the section labeled "Double Probe Response Plots in CUBE."

C. IR Measurements in the CUBE

The IR camera was also used to view the modes generated in the CUBE when the aperture was excited by the incident EM wave. First, the frequencies at which significant modes were produced were determined by sweeping over a frequency range from 2 to 4 GHz. This data was taken and used as a reference to compare the field distributions with a probe present versus the absence of a probe. Both the D-dot and B-dot probes were positioned in the CUBE in all three configurations and tested over the 2-4 GHz range. IR plots of the empty CUBE cavity modes and the IR plots of the field distributions around the probes in the CUBE are contained in Volume II, in the section labeled "CUBE IR Measurements." As was seen in the free-field IR measurements, the D-dot probe disturbed the field much more than the smaller B-dot probe. Because the probes were placed in a region of the CUBE where the field is strong (near the aperture), various differences were observed in the amount of field disturbance for each of the three configurations.

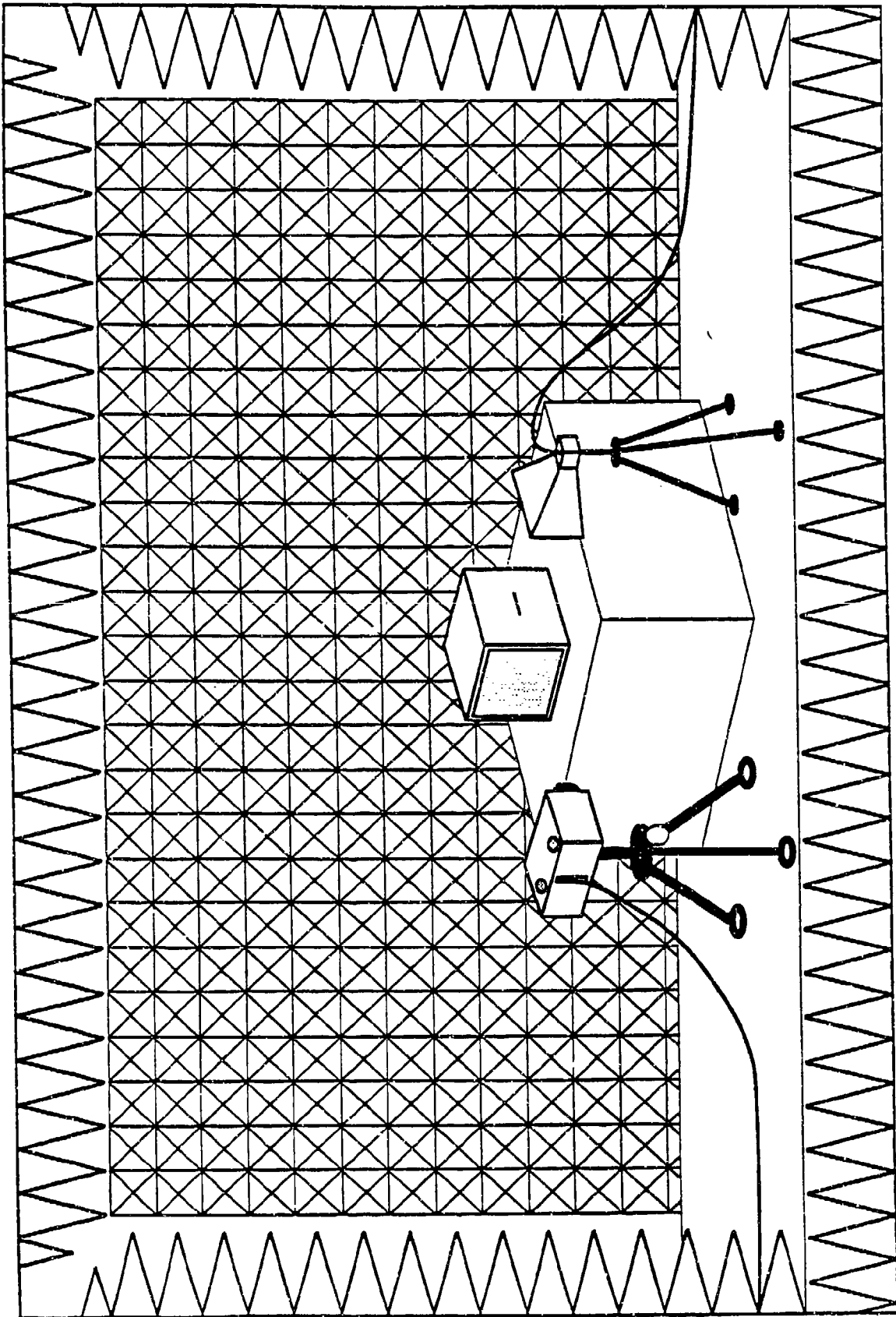


Figure 10 - Cavity (CUBE) Test Set-up

Figures 11-16 contain representative samples of the empty cavity modes; Figures 17-22 contain representative samples of the single B-dot or D-dot probes in configurations A, B and C inside the CUBE for several frequencies between 2 and 4 GHz.

The double probe test was performed with two B-dot probes in configuration A at the mode frequency of 2.708 GHz. The field was disturbed near the probe tips; however, the most disturbance came from the SMA feedlines where coupling was seen.

VI. Data Validation

Several of the single and double probe measurements were repeated at the end of the study to verify the repeatability of the measurements.

Similar setup configurations of rotations were tested. The results of this verification test are contained in Volume II, in the sections labeled "Single Probe Free-Field Verification Measurements" and "Double Probe Free-Field Verification Measurements." Reasonable agreement between the earlier and latter tests were obtained.

VII. FIELDS IN A RECTANGULAR CAVITY EXCITED BY A LONG THIN APERTURE

A. Cavity Effects

In determining the effects of an enclosed region on probe response it is helpful to have an expectation of the fields from analysis. This section describes the expected field structure in terms of both spatial and amplitude terms for a metallic rectangular box with a slit aperture on one side.

The geometry under consideration is shown in Figure 23. The box dimensions are $x_0 = y_0 = 36$ inches and $z_0 = 30$ inches. This box is larger than the one used for the infrared measurements given above. The aperture geometry is shown in Figure 24. The aperture is centered on the $z = z_0$ face of the box and has width $w_d = 25$ cm and height $h_d = 5$ mm.

B. Cavity Fields

There are three steps in finding the fields in the box. First, the incident field on the box must be known or assumed. Second, the coupling of the incident field to the aperture must be determined. This involves finding the equivalent currents in the aperture. Finally, the fields inside the box can be found from the currents by using modal expansions. In this work, the fields in the box are assumed not to change the currents in the aperture.

1. Incident Field

The incident field on the box is assumed to be a 1 V/m wave traveling in the z direction with the electric field polarized in the x direction. All results are calculated using this unity amplitude wave. It should be noted that this is the incident wave only and does not include any scattering. Thus, to compare with experimental measurements, the field in the region which the aperture occupies must be known in the absence of the box.

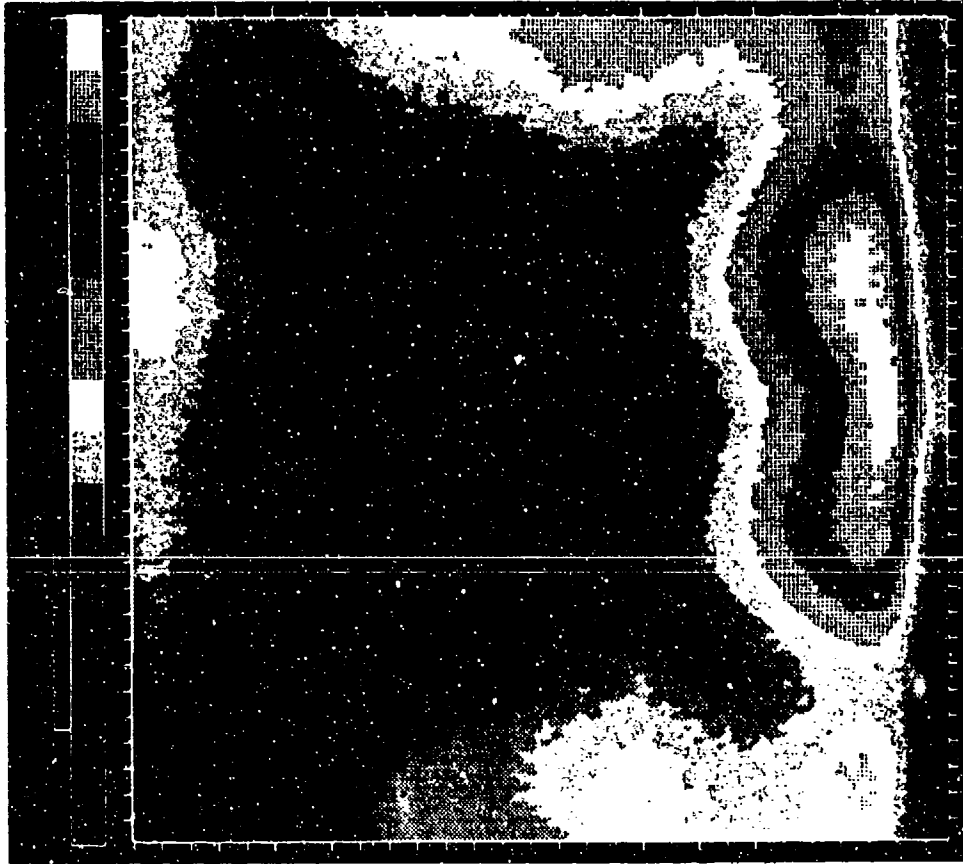


Figure 11: Empty Cavity 2 GHz

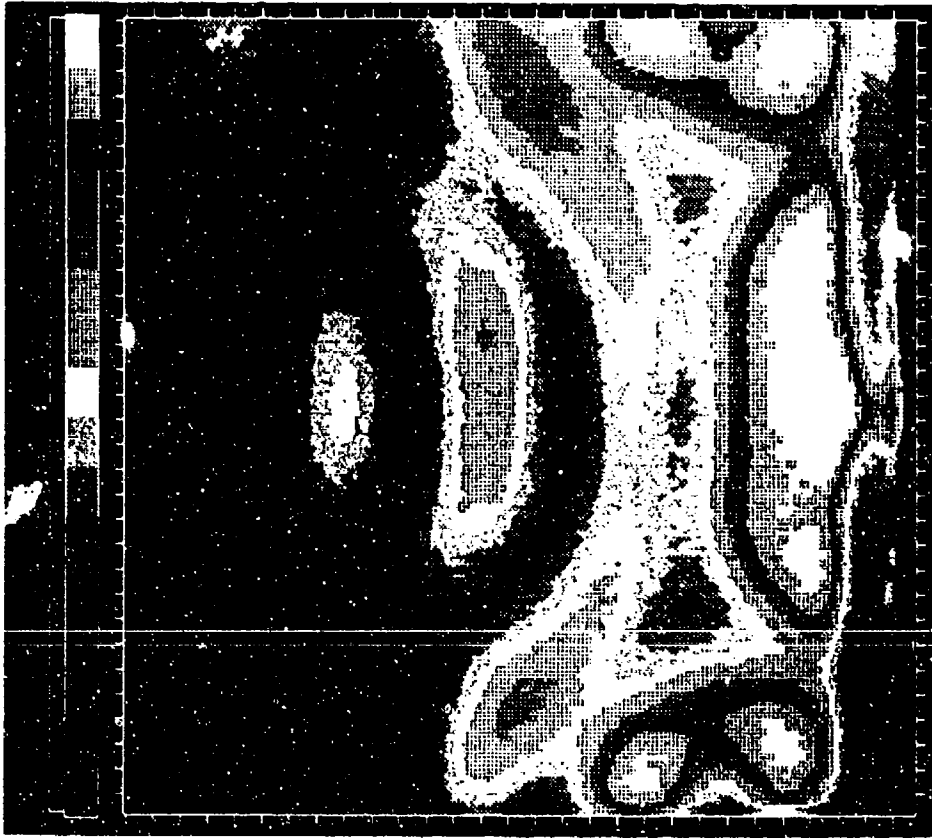


Figure 12: Empty Cavity 2.708 GHz

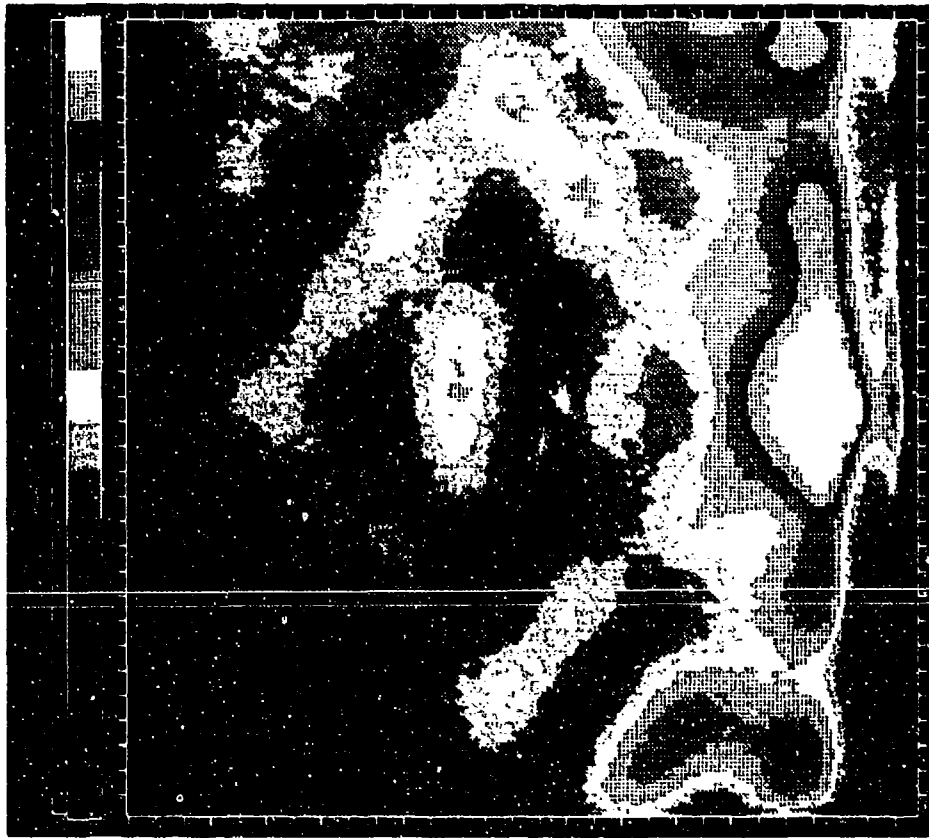


Figure 13: Empty Cavity 2.796 GHz

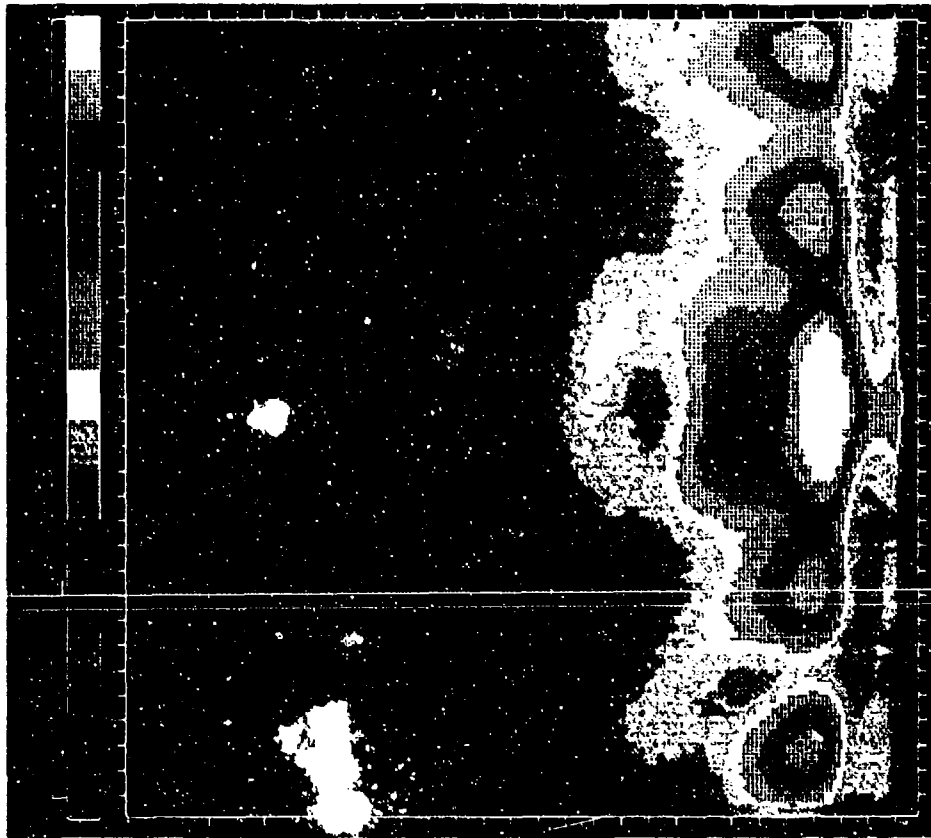


Figure 1 : Empty Cavity 2.890 GHz

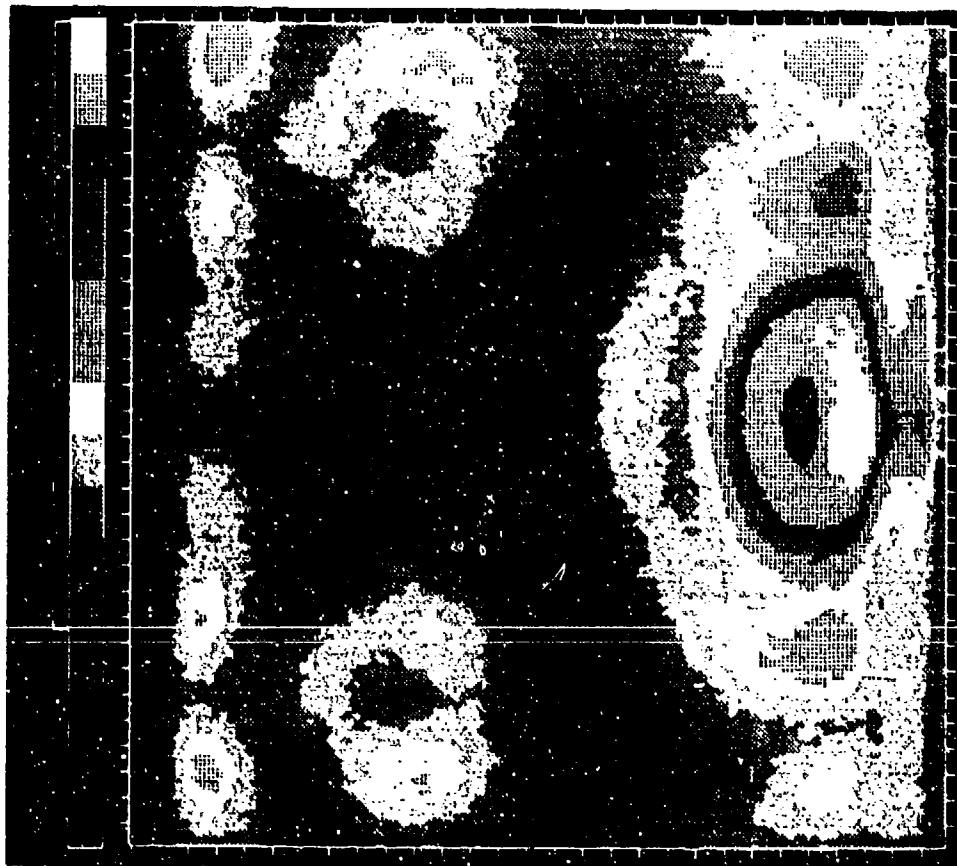


Figure 15: Empty Cavity 3.345 GHz

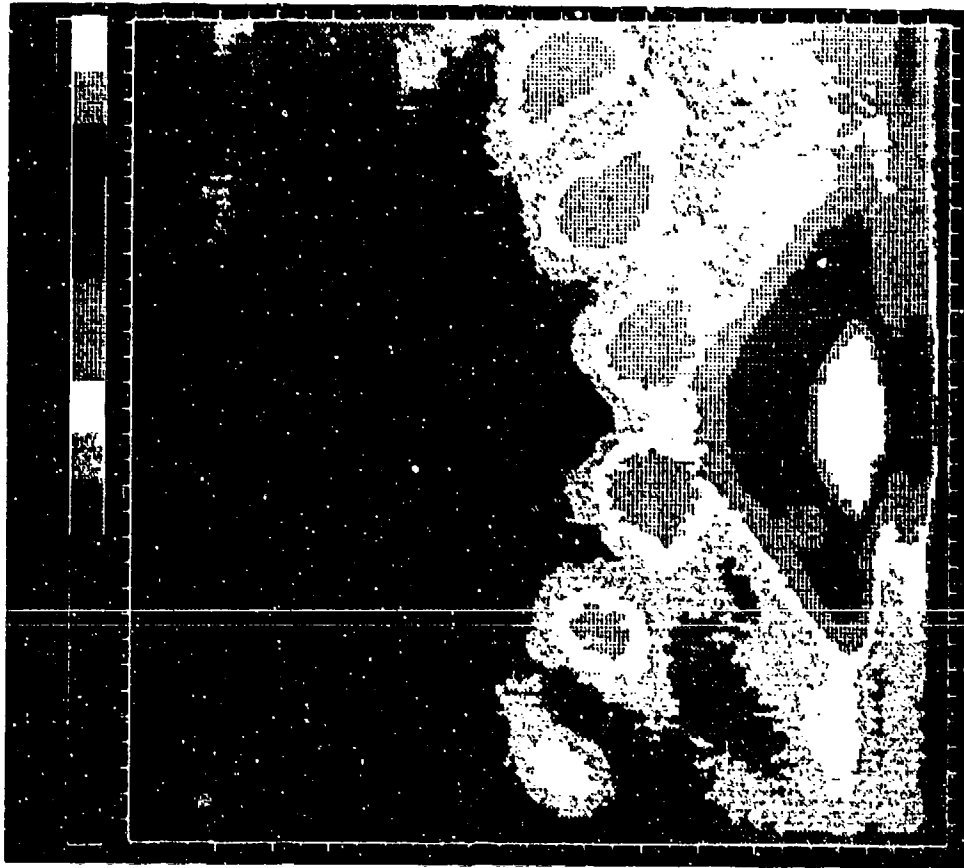


Figure 16: Empty Cavity 3.810 GHz

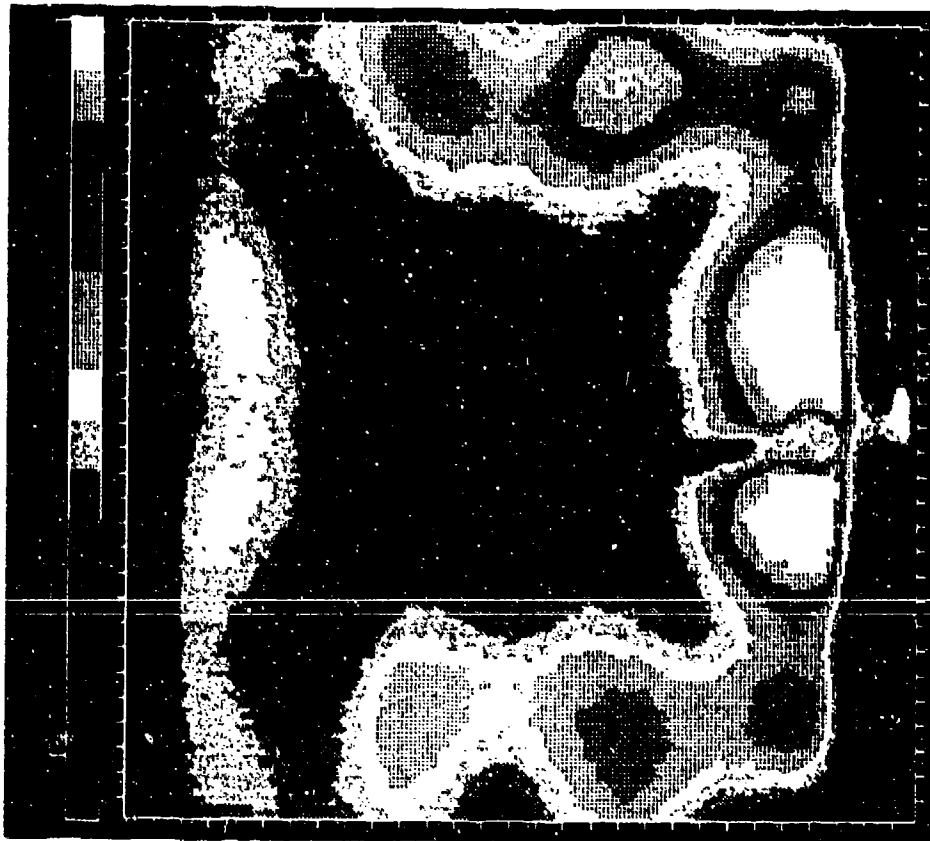


Figure 17a: D-dot Probe Configuration A 2 GHz

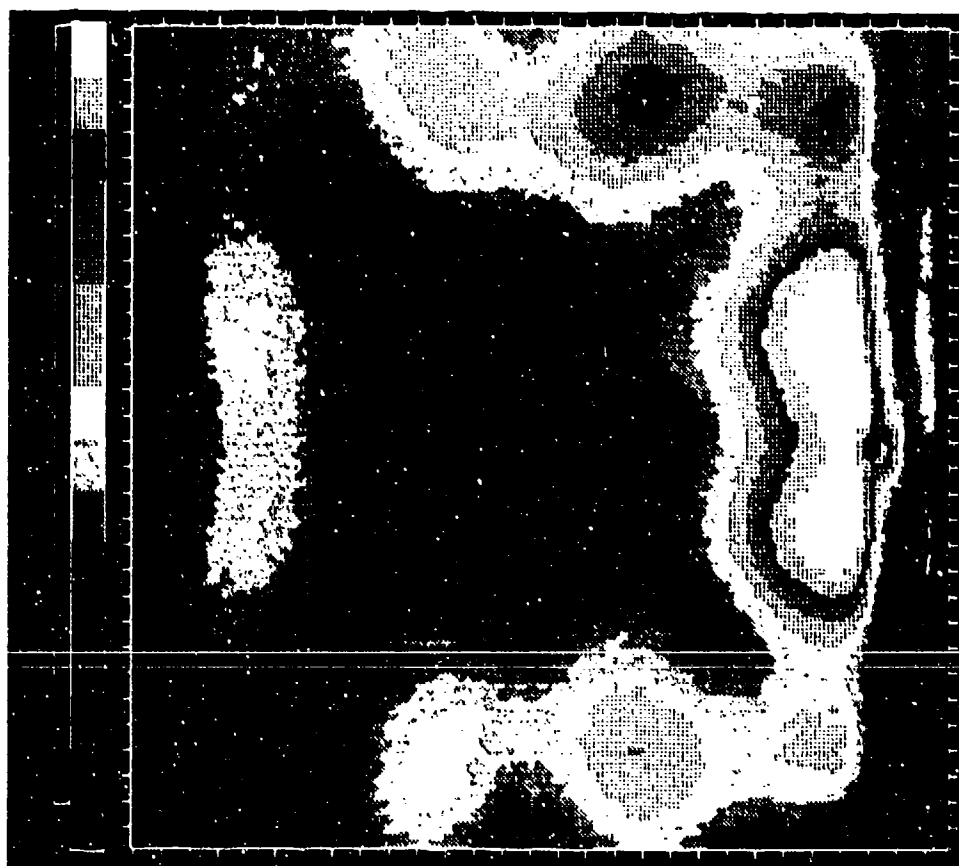


Figure 17b: D-dot Probe Configuration B 2 GHz

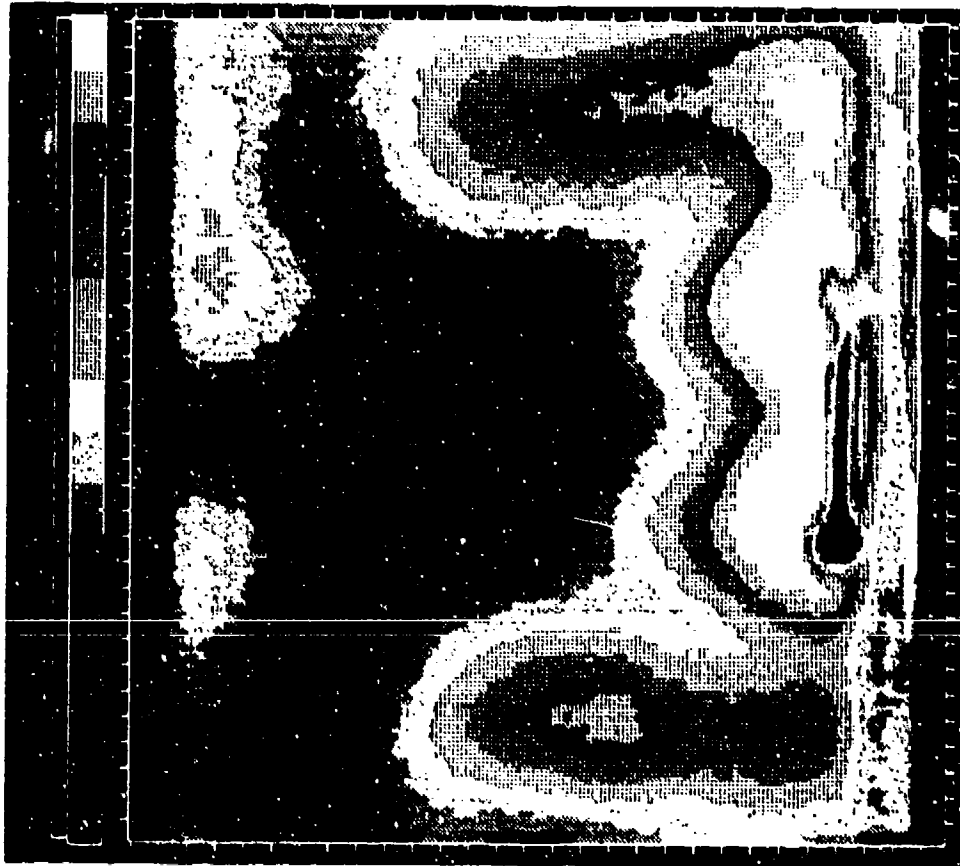


Figure 17c: D-dot Probe Configuration C 2 GHz

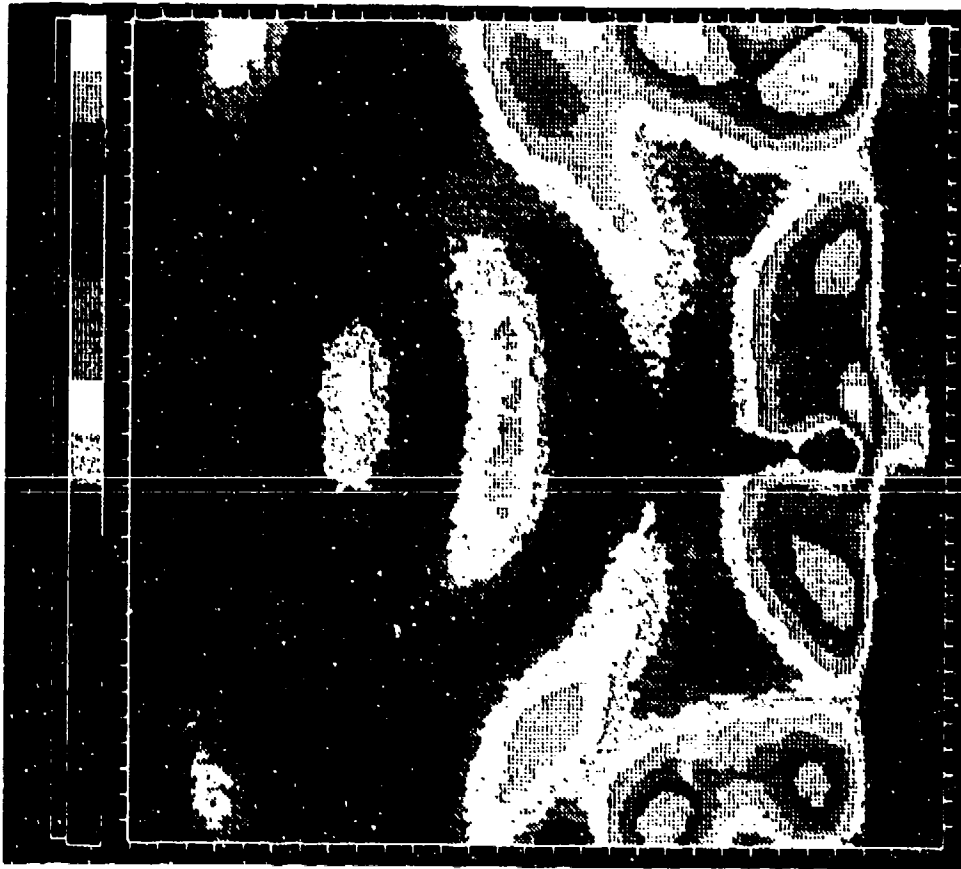


Figure 18a: D-dot Probe Configuration A 2.708 GHz

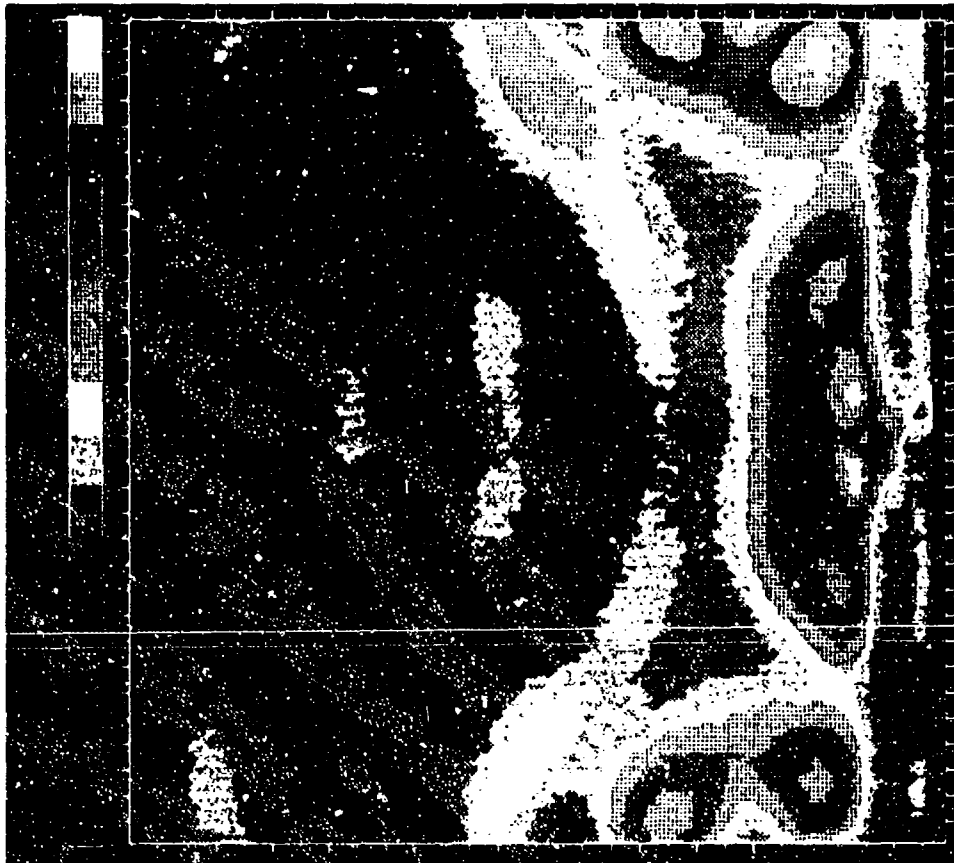


Figure 18b: D-dot Probe Configuration B 2.708 GHz

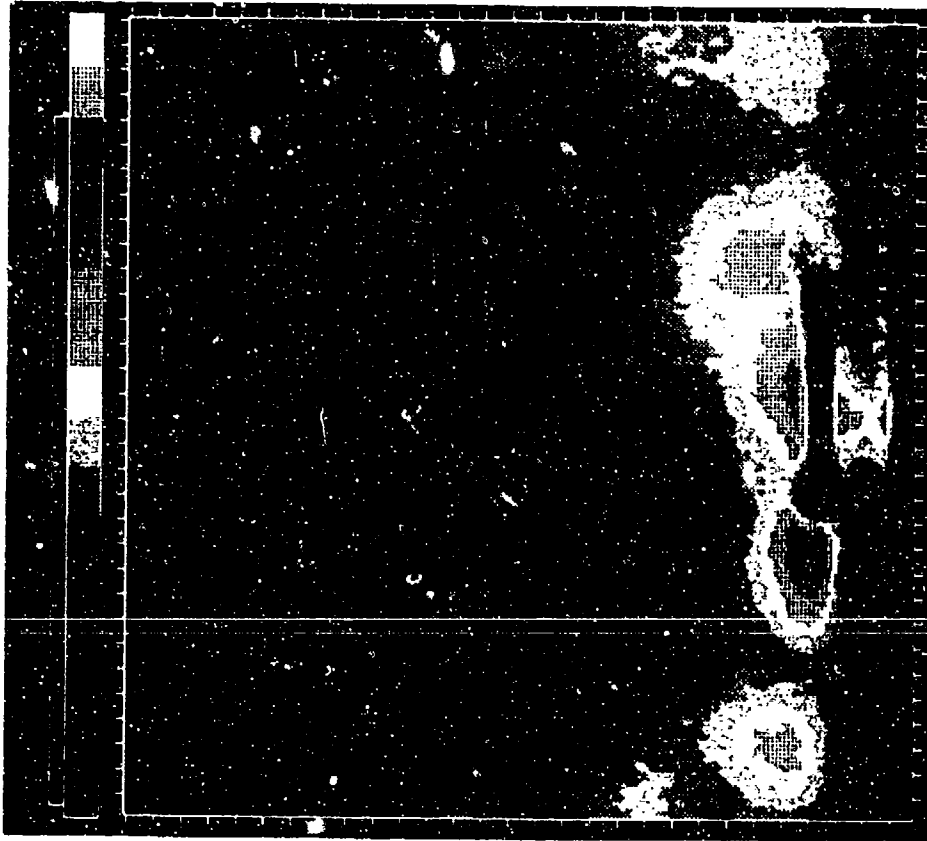


Figure 18c: D-dot Probe Configuration C 2.708 GHz

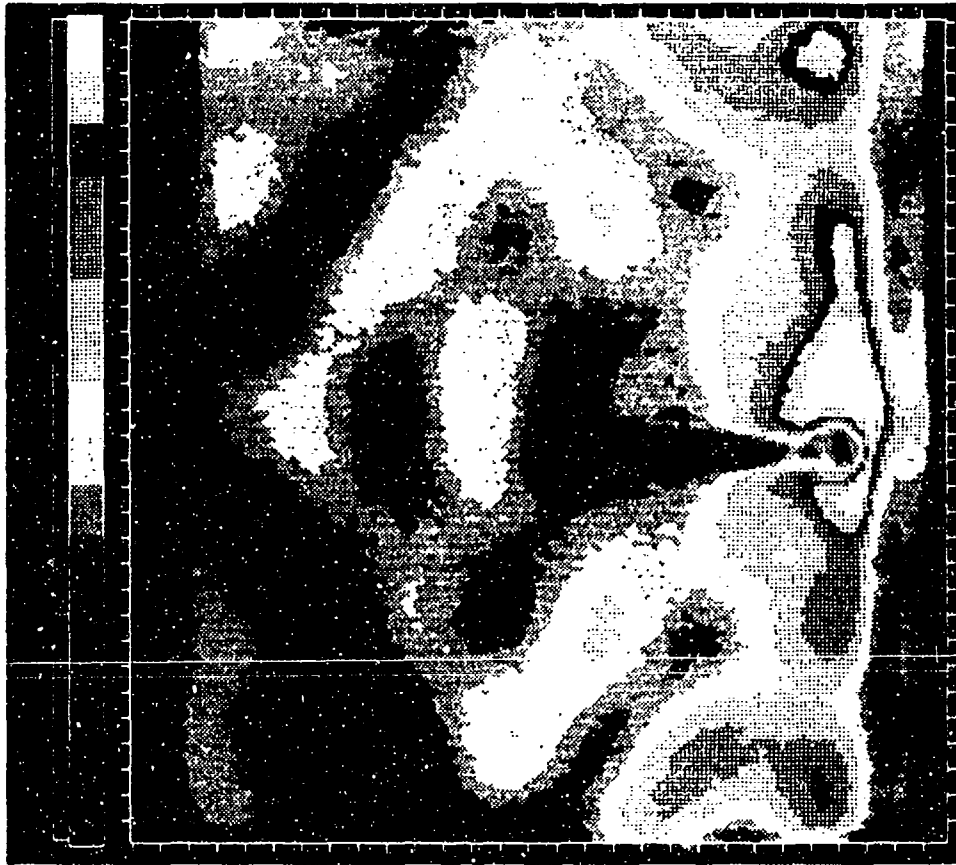


Figure 19a: D-dot Probe Configuration A 2.796 GHz

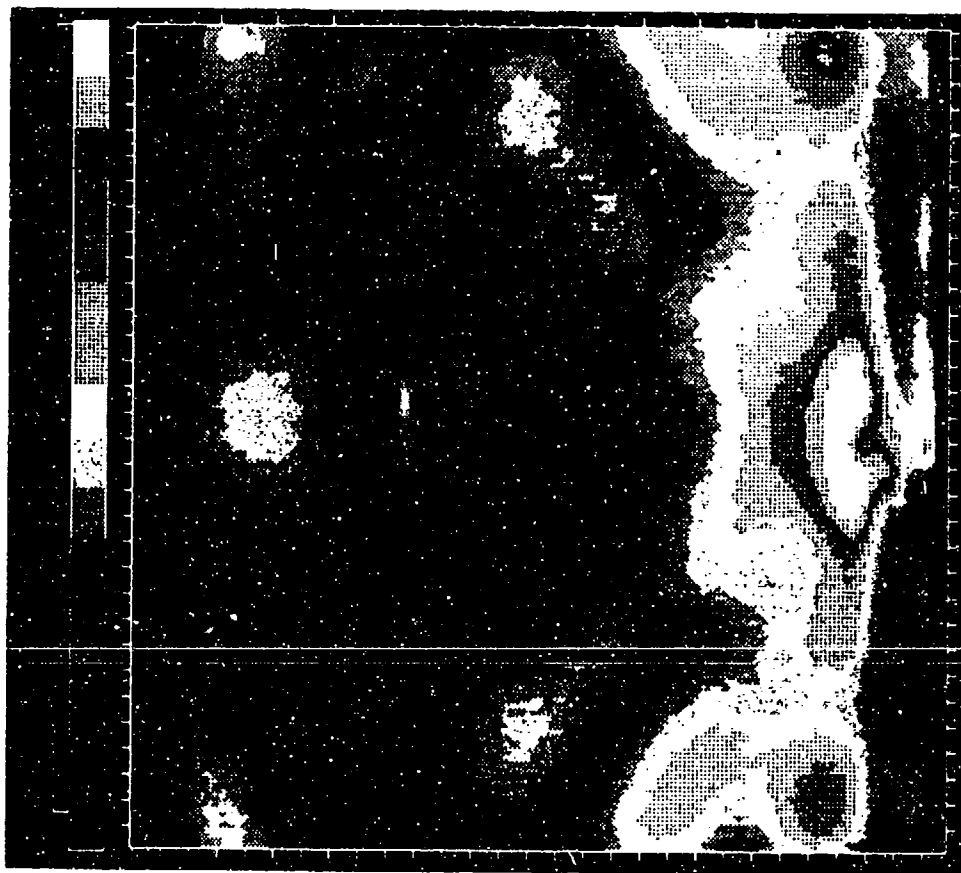


Figure 19b: D-dot Probe Configuration B 2.796 GHz

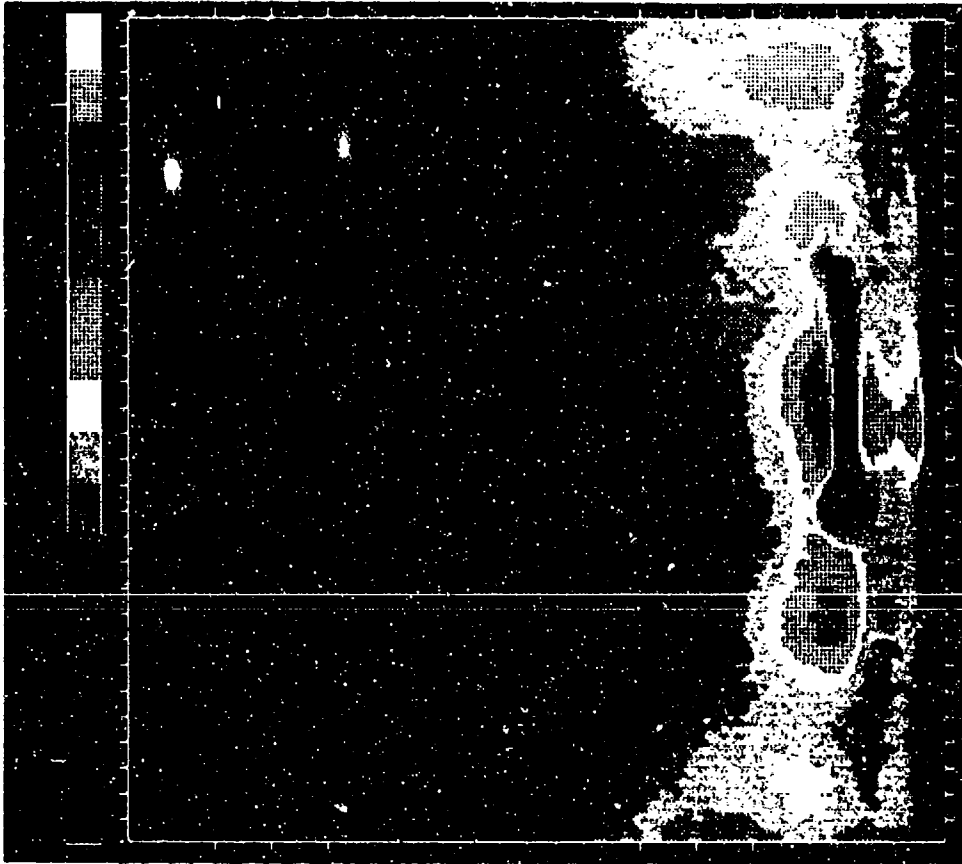


Figure 19c: D-dot Probe Configuration C 2.796 GHz

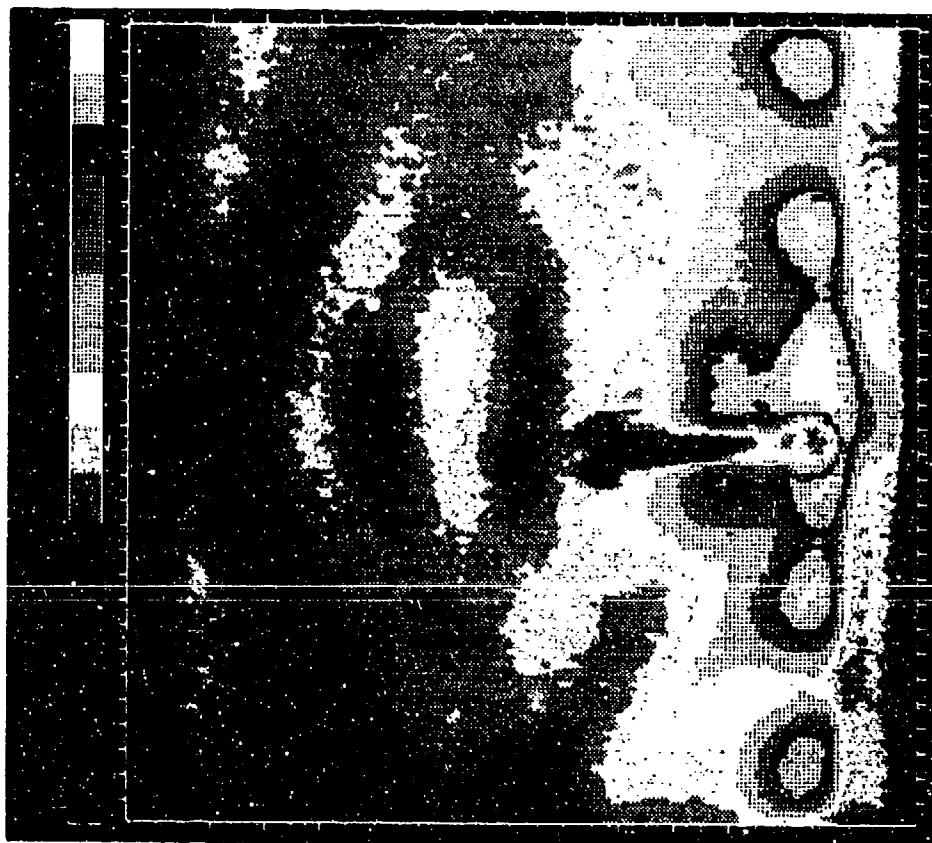


Figure 20a: D-dot Probe Configuration A 2.890 GHz

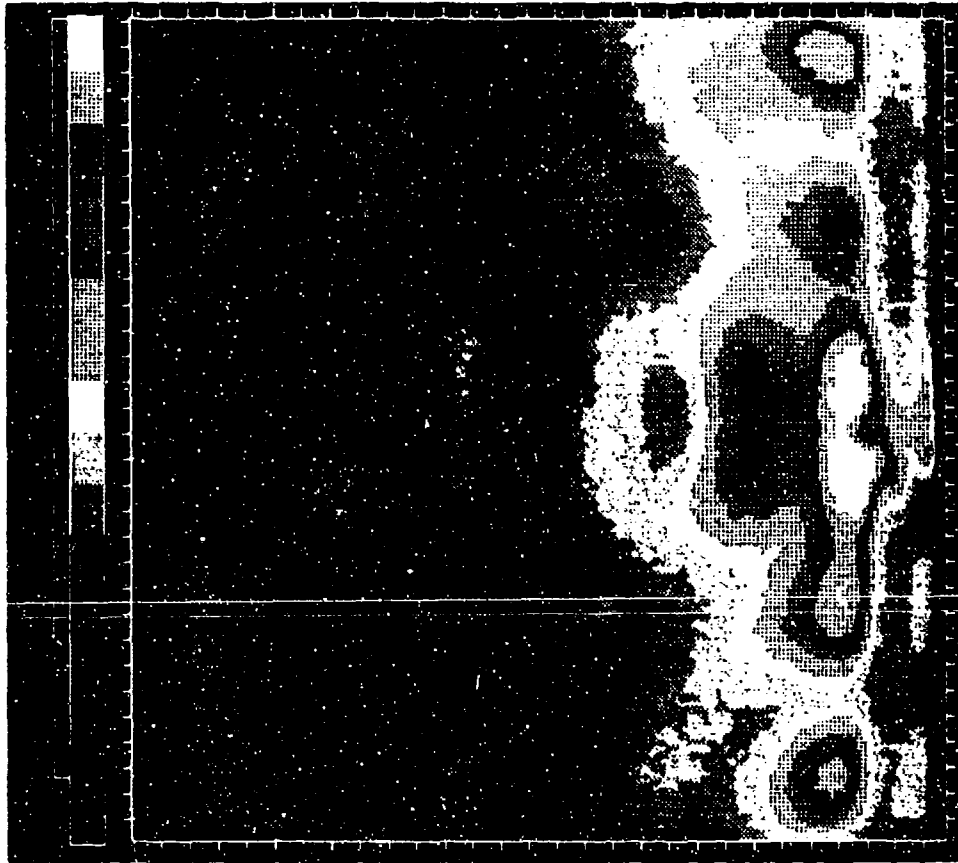


Figure 20b: D-dot Probe Configuration B 2.890 GHz

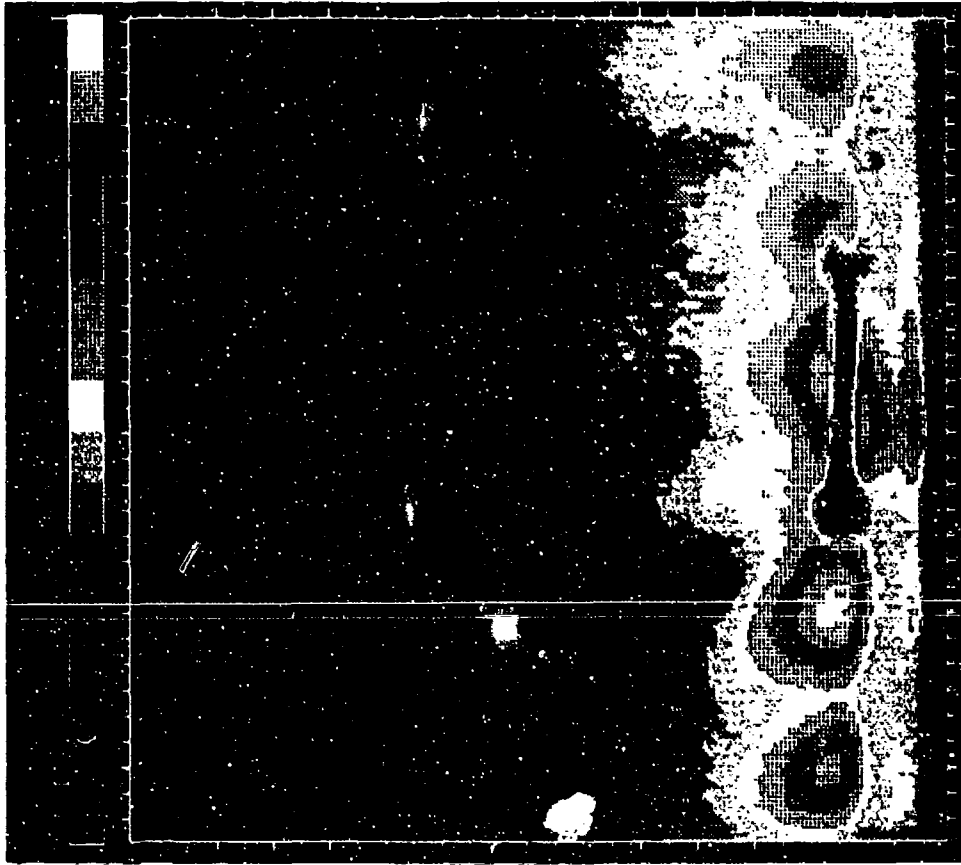


Figure 20c: D-dot Probe Configuration C 2.890 GHz

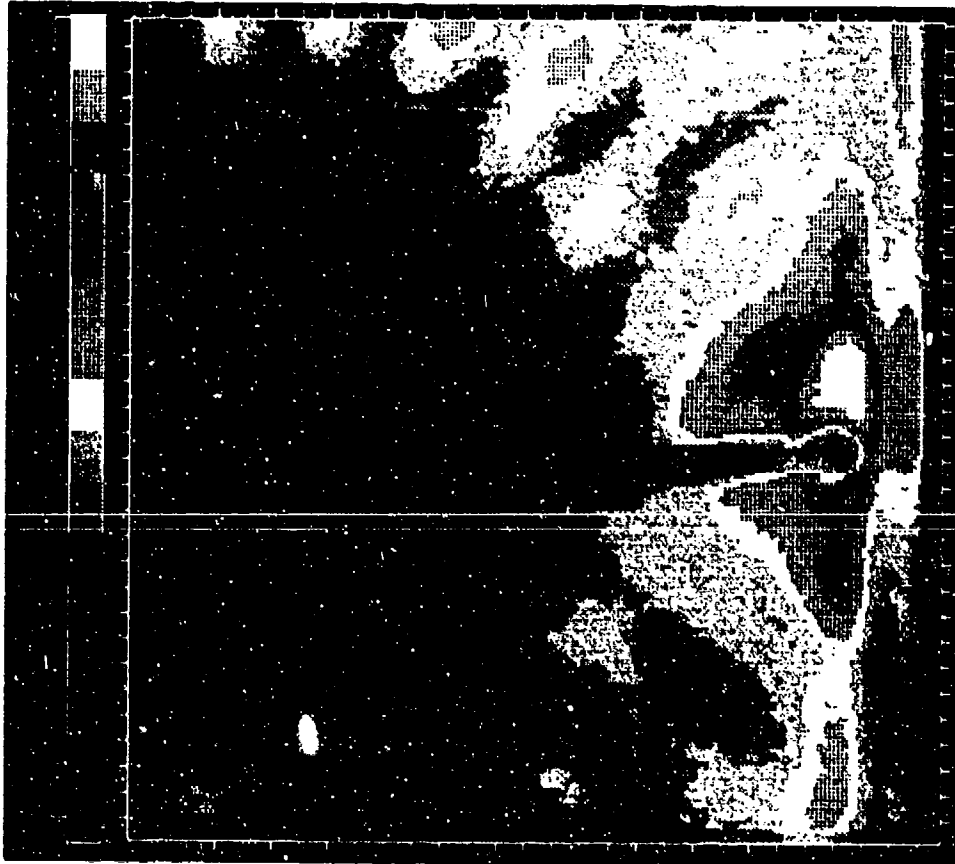


Figure 21a: D-dot Probe Configuration A 3.810 GHz

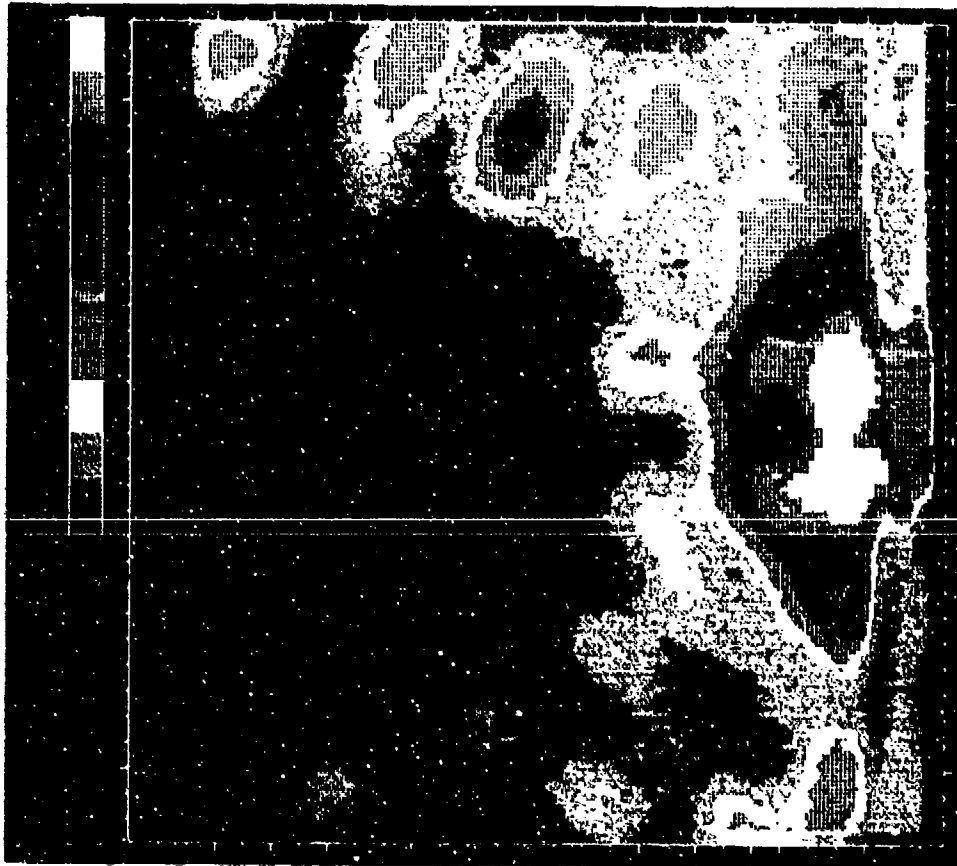


Figure 21b: D-dot Probe Configuration B 3.810 GHz

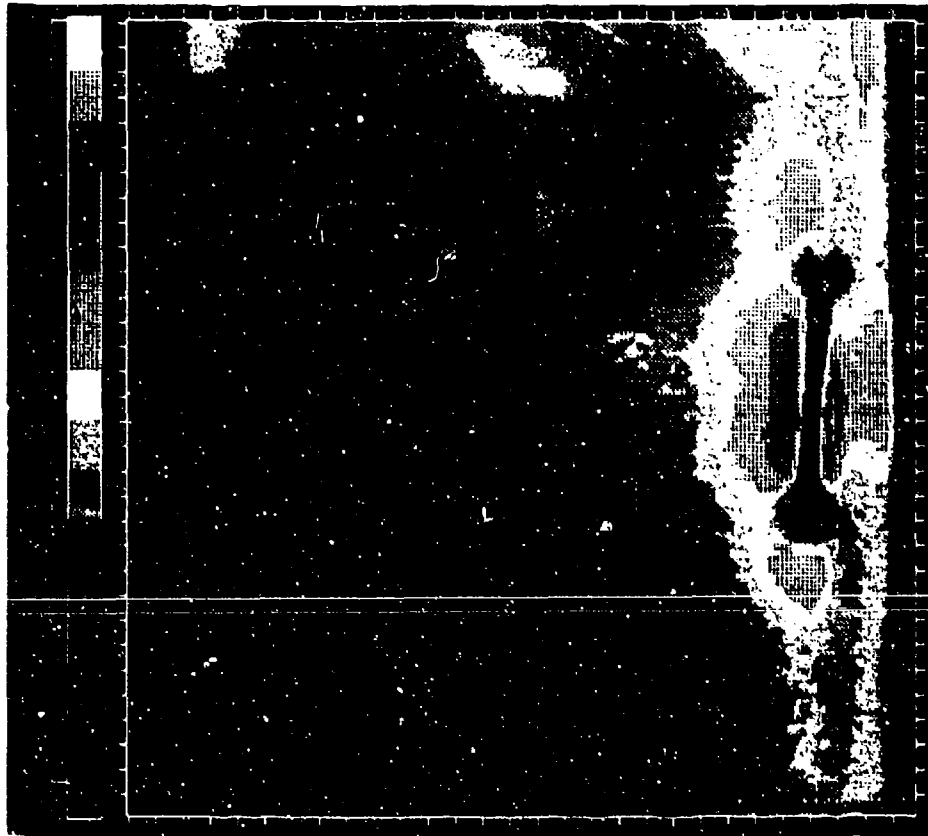


Figure 21c: D-dot Probe Configuration C 3.810 GHz

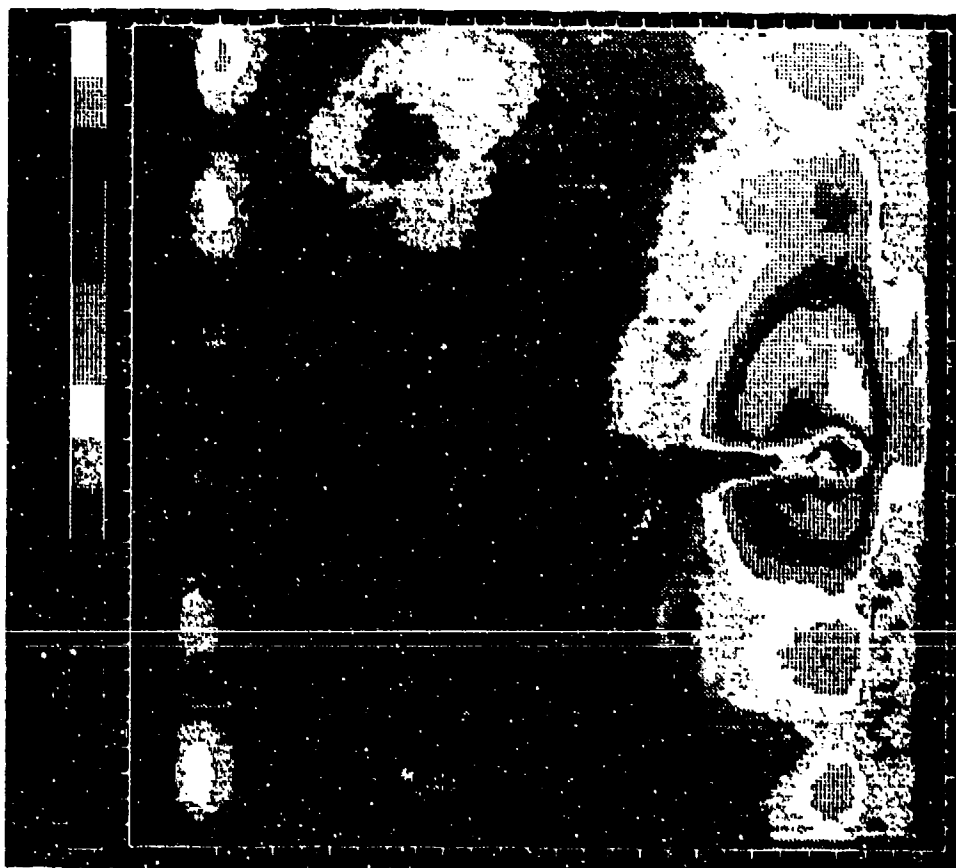


Figure 22a: D-dot Probe Configuration A 3.345 GHz

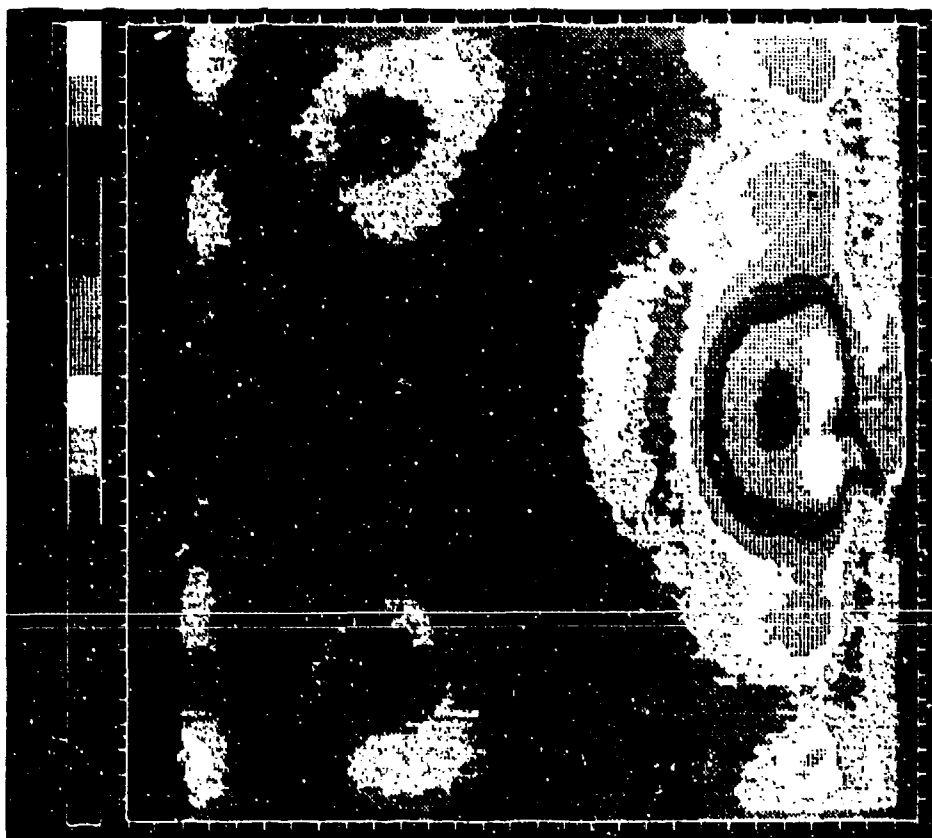


Figure 22b: D-dot Probe Configuration B 3.345 GHz

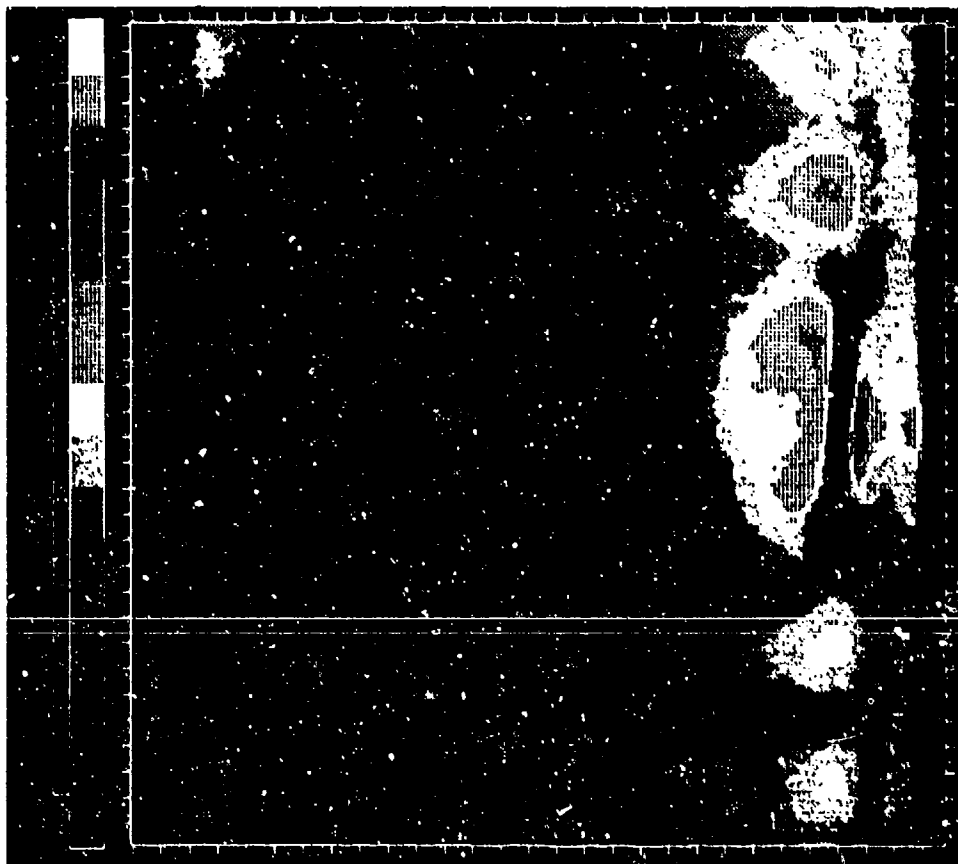


Figure 22c: D-dot Probe Configuration C 3.345 GHz

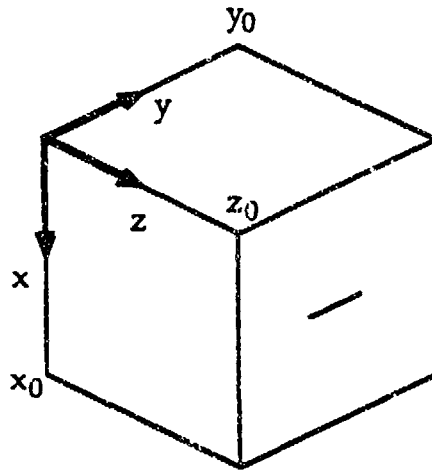


Figure 23: Cavity geometry.

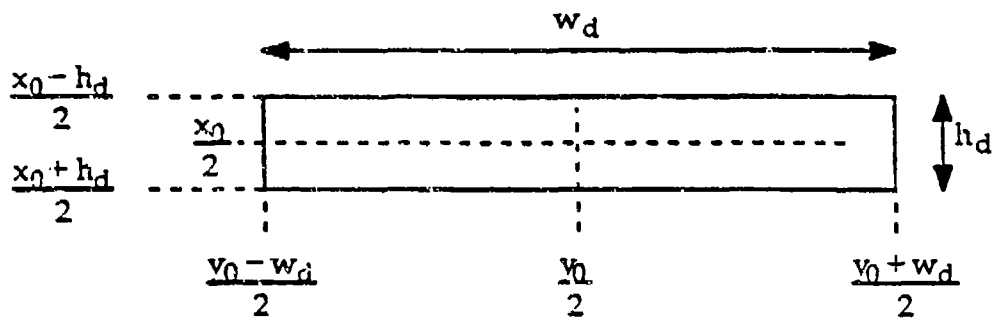


Figure 24: Aperture geometry.

2. Coupling to a Slit Aperture

The slit aperture is assumed to be situated in a perfect electric conducting (PEC) infinite plane with infinitesimal thickness. In reality, the aperture is on the side of a box with finite thickness. However, these two approximations simplify the analysis and provide a good first-order solution.

A slit in an infinitesimally thin, infinite PEC plane can be analyzed by considering its dual: an infinitesimally thin PEC strip in free space. Butler [ref. 9] has further shown that the strip can be approximated by wire of circular cross section whose radius is 1/4 that of the strip width and whose length is the same as the strip. Therefore, rather than analyze the slit aperture, it is permissible to analyze a wire of the same length with a radius 1/4 that of the slit width. The surface electric current density J (A/m) found for the wire from a unity amplitude magnetic field is the same as the surface magnetic current density M (V/m) in the slit from a unity amplitude electric field. With this approximation of a wire for the slit, it is possible to find the amplitude of the magnetic current in the slit.

The spatial distribution of the magnetic currents in the slit is assumed to be a half sinusoid along the length and a constant from side to side. Harrington [ref. 10] has shown that for slits in infinite PEC planes and for frequencies such that the slit length is less than or equal to $3/4\lambda$, the half sinusoid is a good approximation. Further, recall that the box has some finite thickness and looks more like an aperture in a plane, followed by a short section of waveguide and then another aperture. The approximation used here for the spatial current distribution is the same as for the dominant mode of a waveguide. Thus, the finite thickness of the box sides helps to constrain the current to the assumed distribution.

In order to check these assumptions concerning the current amplitude and spatial distribution, several computer simulations of a wire were performed with the Numerical Electromagnetics Code (NEC). The wire length was the same as that of the slit (25 cm) while its radius was 1/4 the slit width (radius of 1.25mm). Figure 25 shows the calculated electric current magnitude and phase angle on the wire, normalized to the incident magnetic field for a frequency of 600 MHz. At this frequency, the wire is a half wavelength long. The horizontal scale shows the position along the wire; the left vertical scale is the surface electric current density J (A/m) normalized to the incident magnetic field H_i (A/m); the right vertical scale is the phase angle of the current in degrees. Both the distribution of current along the wire and the amplitude agree very well with calculations by Harrington [ref. 10], when scaled to the same slit width.

Figure 26 shows the ratio J/H_i for the slit at various frequencies of excitation. By using linear interpolation of this data, the magnetic current in the slit can be found for a 1 V/m incident plane wave at a frequency in the given range.

Using the approximations above, the magnetic current in the slit aperture can be expressed as

$$\vec{M} = \delta(z-z_0)[P(x_1, x_2)] \left[\sin \left[\pi \frac{y-y_1}{y_3-y_1} \right] \right] \quad (y_1 \leq y \leq y_3)$$

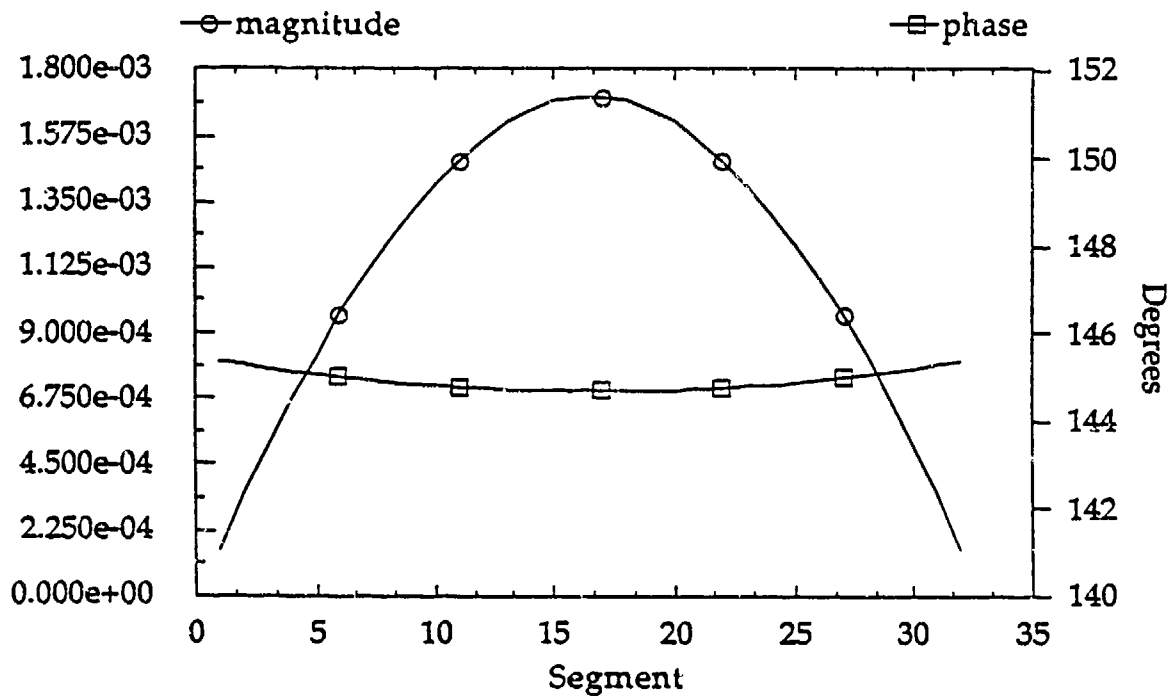


Figure 25: Current magnitude and phase on a wire of length $\lambda/2$ and radius $\lambda/400$ (1/4 the slit width) normalized to the incident magnetic field.

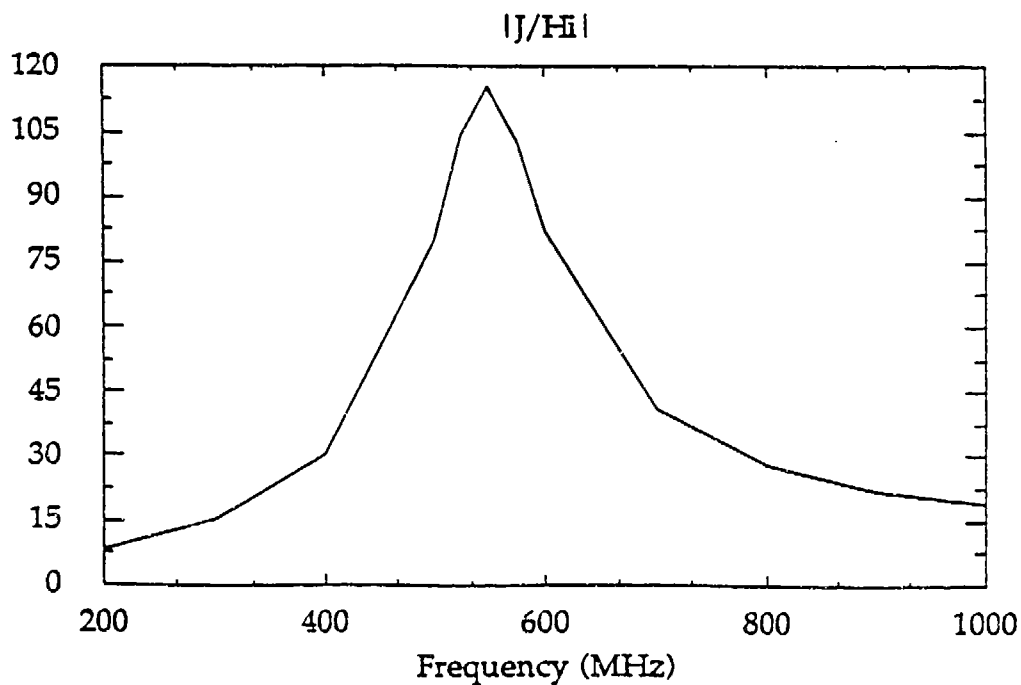


Figure 26: $|J/H_i|$ for the slit at various frequencies of excitation.

where

δ is the delta function

$P(a,b)$ is a square pulse from a to b

$$x_1 = X_0 - \frac{h_d}{2}$$

$$x_2 = x_0 + \frac{h_d}{2}$$

h_d is the slit height (extent in the x direction)

$$y_1 = \frac{y_0 - w_d}{2}$$

$$y_3 = \frac{y_0 + w_d}{2}$$

w_d is the slit width (extent in the y direction)

3. Modal Expansions

Because of the boundary conditions imposed by the walls of the box, the electromagnetic fields can exist only in certain defined forms called modes. These are similar to the propagating modes in waveguides with one major difference. In a waveguide, a given mode may exist if the frequency of operation is above the cutoff frequency of that mode; in a cavity, a mode can exist only in a small range of frequencies about its resonance frequency. For the geometry being considered here, there will be some small leakage fields in the region of the aperture when the frequency of operation is not close to any resonance frequency.

However, there will be significant amplitude fields if the frequency of operation is close to a resonance frequency. The amplitude of the fields inside the cavity depends on the assumed distribution of magnetic current in the aperture. Each mode is excited with a different amplitude depending on the agreement between the modal field structure and the source current. This agreement is modeled by the coupling coefficient. A larger value of the coupling coefficient produces larger field levels inside the cavity.

With the current in the aperture as described above, the transverse electric (TE), y -axial modes are excited. These fields take the form

$$E_x^{TE_y} = -cj\omega\mu k_x \cos(k_x x) \sin(k_y y) \sin(k_z z)$$

$$E_y^{TE_y} = 0$$

$$E_z^{TE_y} = cj\omega\mu k_x \sin(k_x x) \sin(k_y y) \cos(k_z z)$$

and

$$\begin{aligned} H_x^{TE_y} &= -ck_x k_y \sin(k_x x) \cos(k_y y) \cos(k_z z) \\ H_y^{TE_y} &= c(k_x^2 + k_y^2) \cos(k_x x) \sin(k_y y) \cos(k_z z) \\ H_z^{TE_y} &= -ck_y k_z \cos(k_x x) \cos(k_y y) \sin(k_z z) \end{aligned}$$

where:

$$\begin{aligned} \omega &= 2\pi f \\ \mu &= 4\pi \times 10^{-7} \text{ H/m} \\ k_x &= \frac{m\pi}{x_0} \quad (m = 0, 1, 2, \dots) \\ k_y &= \frac{n\pi}{y_0} \quad (n = 1, 2, 3, \dots) \\ k_z &= \frac{p\pi}{z_0} \quad (p = 0, 1, 2, \dots) \end{aligned}$$

and m and p are not both 0 and c is the coupling coefficient

The coupling coefficient of each mode is given as

$$c = \frac{8j}{\omega\mu(k_x^2 - k_b^2)x_0 y_0 z_0} X(m)Y(n)Z(p)$$

where

$$\begin{aligned} k^2 &= \omega^2 \mu \epsilon \\ \epsilon &= 8.854 \times 10^{-12} \text{ F/m} \\ k_b^2 &= k_x^2 + k_y^2 + k_z^2 \\ X(m) &= \begin{cases} \frac{\sin(k_x x^2) - \sin(k_x x^2)}{k_x} & m = 0 \\ h_d & m = 0 \end{cases} \end{aligned}$$

$$Y(n) = \frac{\sin(ay_3 - b) - \sin(ay_1 - b)}{2a} + \frac{\sin(dy_1 - b) - \sin(dy_3 - b)}{2d}$$

$$a = \frac{\pi}{y_3 - y_1} - k_y$$

$$b = \frac{\pi y_1}{y_3 - y_1}$$

$$d = \frac{\pi}{y_3 - y_1} + k_y$$

x_1, x_2, y_1 and y_3 are as given previously and

$$Z(p) = \cos(p\pi)$$

It can be seen from the above equations that the variation with p is simply a sign change of $Z(p)$. The variation with n results in all even values of n producing a $Y(n)$ equal to zero. The variation with m results in all odd values of m producing an $X(m)$ equal to zero. It should be noted that, because k_p depends on the mode numbers, m, n and p , the variation of the coupling coefficient with the mode numbers is more complex than that which arises from $X(m), Y(n)$ and $Z(p)$. The resonance frequencies are given as

$$f_r = \frac{1}{2\pi\sqrt{\mu\epsilon}} \sqrt{k_x^2 + k_y^2 + k_z^2}$$

A summary of the resonance frequencies and magnitude of the coupling coefficients for the modes with the lowest resonance frequencies is given in table 1. The coefficients from table 1 are plotted in Figure 27. As can be seen, the mode number n separates the coefficients into families of curves with the $n=1$ curve being the most efficient.

In addition to the resonance frequency and coupling coefficient, each mode has a unique value of Q . Q models the losses in the cavity which arise from the finite conductivity of the walls and leakage through apertures. A calculation of Q considering only wall losses is listed in table 1 for various modes. The values calculated are much higher ($\approx 10^5$) than the total Q for real systems, indicating that leakage is the dominant loss mechanism. Figure 28 shows the variation of the maximum value of the x component of the electric field with Q for the $m=2, n=1$ and $p=2$ mode, which resonates at approximately 538 MHz. For this figure, the value of Q was set and then the maximum value of the electric field was calculated. The Q 's for real cavities are typically on the order of 10's to 100's. As is evident from Figure 28, these are the values of Q which have the most significant impact on the field level generated in the cavity. It is possible to measure the cavity Q , however that was not done in this work. For all results which follow, the Q for wall losses only was used to determine the field levels in the cavity.

C. Approach Summary

There were several approximations made in order to estimate the fields inside the cavity. First, the aperture was modelled as an aperture in an infinite PEC plane of infinitesimal thickness. Second, the aperture was further modelled as a wire with radius $1/4$ the strip width. This allowed the surface magnetic current along the aperture to be determined. The amplitude of the current in the aperture as a function of frequency was found by considering the current on an equivalent wire at the same frequency. Third, the current was approximated by a spatial distribution of a half-sinusoid along the length and a constant from side-to-side. Fourth, the only modes theoretically allowed by the chosen distribution were the TE, y -axial modes. The coefficients of these modes were determined by appropriate integrals over the region of match (the aperture). Finally, the Q for each mode was calculated taking into account wall losses only. Although the values obtained were high, these values were used pending further measurements of the true cavity Q 's.

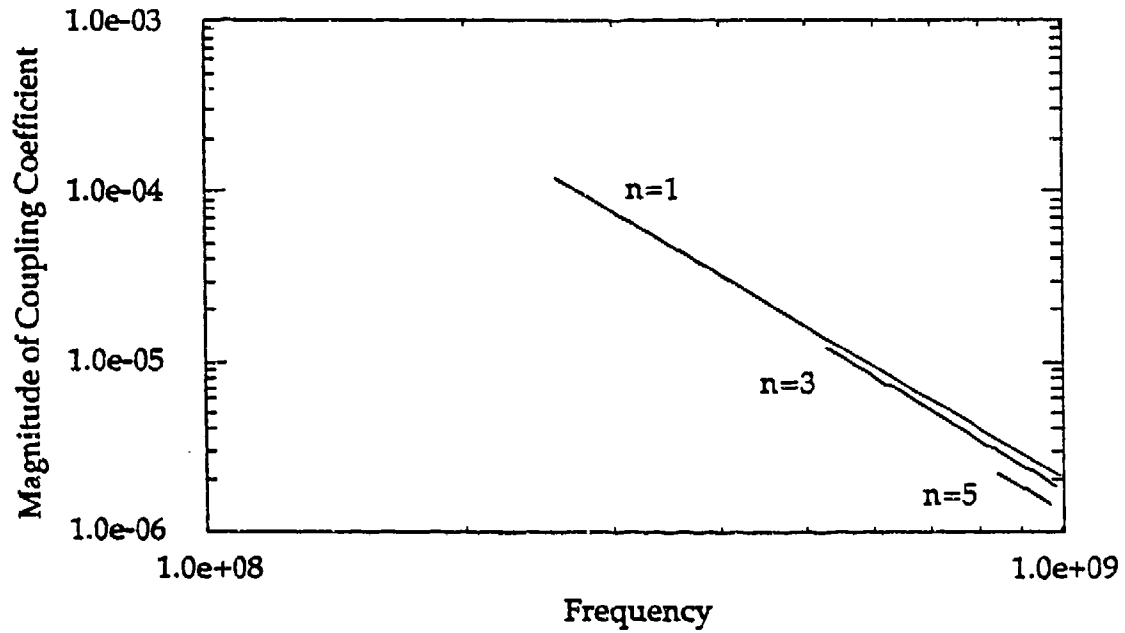


Figure 27: Magnitude of the coupling coefficient as a function of frequency and mode number n .

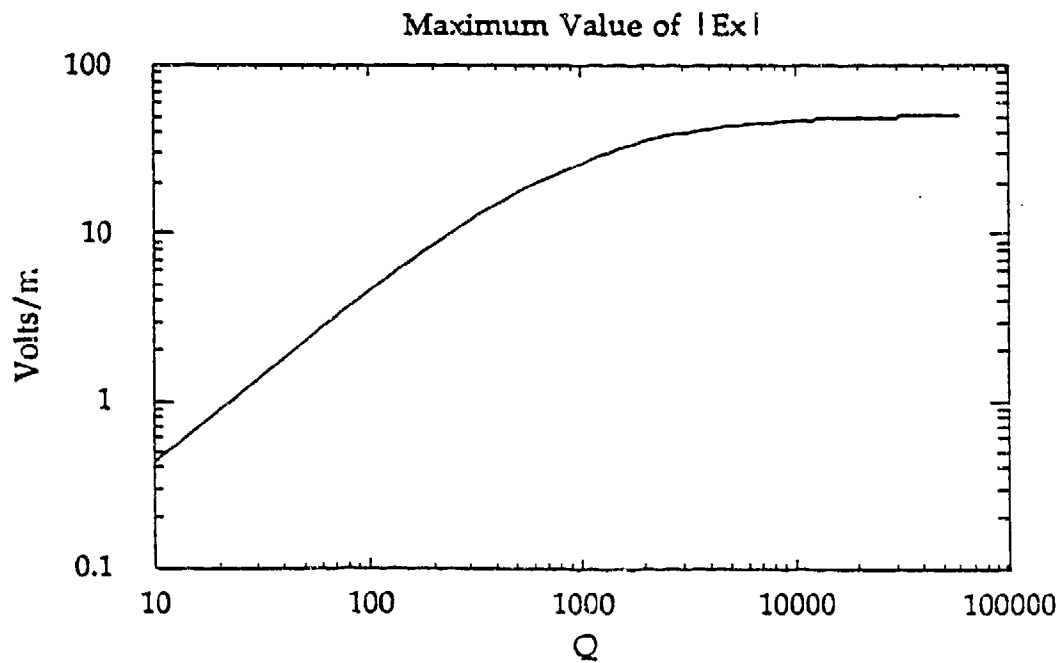


Figure 28: Variation of maximum field value with Q for the 212 mode.

m	n	p	Resonance Frequency	Coupling Coefficient	Q from wall losses
0	1	1	2.5624E+08	1.2191E-04	5.4277E+04
2	1	0	3.6681E+08	4.1475E-05	4.7229E+04
2	1	1	4.1629E+08	2.8403E-05	5.1146E+04
0	1	2	4.2651E+08	2.6513E-05	7.0025E+04
2	1	2	5.3809E+08	1.3181E-05	5.9520E+04
0	1	3	6.1291E+08	8.9500E-06	8.3944E+04
4	1	0	6.7636E+08	6.6402E-06	6.4132E+04
2	1	3	6.9519E+08	6.1209E-06	6.8621E+04
4	1	1	7.0442E+08	5.8801E-06	6.5890E+04
4	1	2	7.8260E+08	4.2910E-06	7.0513E+04
0	1	4	8.0430E+08	3.9644E-06	9.6162E+04
2	1	4	8.6864E+08	3.1417E-06	7.7299E+04
4	1	3	8.9789E+08	2.8442E-06	7.6733E+04
6	1	0	9.9782E+08	2.0719E-06	7.7896E+04
0	1	5	9.9782E+08	2.0784E-06	1.0711E+05
0	3	1	5.3003E+08	1.1985E-05	7.8063E+04
2	3	0	5.9146E+08	8.6017E-06	5.9972E+04
2	3	1	6.2335E+08	7.3488E-06	6.1741E+04
0	3	2	6.3023E+08	7.1351E-06	8.5122E+04
2	3	2	7.1051E+08	4.9672E-06	6.6301E+04
0	3	3	7.6872E+08	3.9351E-06	9.4011E+04
4	3	0	8.2020E+08	3.2304E-06	7.0624E+04
2	3	3	8.3580E+08	3.0541E-06	7.2302E+04
4	3	1	8.4350E+08	2.9708E-06	7.1847E+04
4	3	2	9.0980E+08	2.3688E-06	7.5200E+04
0	3	4	9.2854E+08	2.2341E-06	1.0332E+05
2	3	4	9.8479E+08	1.8688E-06	7.8795E+04
0	5	1	8.4350E+08	2.1956E-06	9.8477E+04
2	5	0	8.8339E+08	1.9064E-06	7.3293E+04
2	5	1	9.0505E+08	1.7728E-06	7.4231E+04
0	5	2	9.0980E+08	1.7502E-06	1.0227E+05
2	5	2	9.6715E+08	1.4534E-06	7.6849E+04

Table 1: Resonance frequencies, magnitudes of the coupling coefficients and Q's for various values of m, n and p.

D. Analytical Results

Figures 29 and 30 show the magnitude of the x component of the electric field, $|E_x|$, in the $y=y_0/2$ plane for the 212 mode at resonance (538 MHz). Figure 29 shows constant magnitude contours spaced in 3 dB increments. The maximum field level is 50.75 V/m. The aperture is at the center right of the figure with its length normal to the paper. Figure 30 shows a three dimensional relief map of the same data.

VII. SUMMARY

Examination of the physical dimensions and construction of the probes, reveals that the D-dot probe is the sturdier of the two probes. The problem encountered during the experiment was that caution had to be taken while handling the B-dot probes more so than the D-dot probes. The SMA connections for the D-dot configuration could be connected without any distortion of the probe itself. Unlike the D-dot probe, the B-dot probe required care to assure that the probe would not be bent while making any SMA connections. The sensor portion of both probes were found damaged on receipt. Both had to be repaired and handled with care.

Repeatability is an important issue. The rotation of the probes by 180° in the free field case should not result in the large power difference observed. Internally, the B-dot and D-dot probes were not symmetric relative to their two output terminals. The connections were made using a calibrated torque wrench. For the single probe measurements, configuration A provided the best results for both probes because the body of each probe and the SMA cable were almost completely isolated from the incident E and H fields. This resulted in very little reflection that would produce interference.

The degree of rotation of the probe angle was a key factor in determining the probe performance. The D-dot probe had to be positioned horizontal, with respect to the vertical E-field from the horn (defined as 0° and 180° probe rotation angles), so that the E-field was parallel to the dipole sensor. When the D-dot probe was positioned vertically (defined as 90° and 270° probe rotation angles), the measured field intensities were considerably less, as expected. The B-dot probe had to be positioned vertically for best performance and sensitivity. This is because the H-field, which is orthogonal to the E-field and direction of propagation, will be incident parallel to the axis of the cylindrical sensor portion of the probe in that position. In the 0° and 180° probe rotation angles, the B-dot measurements were less, as expected.

Configuration B provided good performance for the B-dot probe at 90° and 270° probe rotation angles. The performance was slightly degraded because of interference from the body of the probe and the system cable. The D-dot probe is unusable in Configuration B.

Configuration C provided good performance for the D-dot probe at 0° and 180° probe rotation angles, but, again, the performance was slightly degraded because of the body of the probe and the system cable. The B-dot probe is unusable in Configuration C.

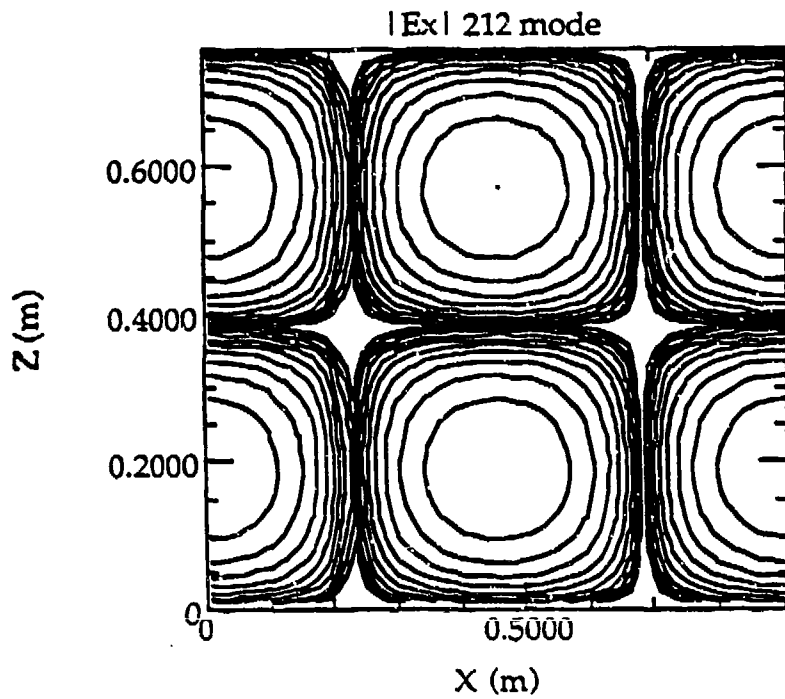


Figure 29: Constant magnitude contours spaced in 3 dB increments for the 212 mode at resonance (538 MHz), in the $y=y_0/2$ plane.

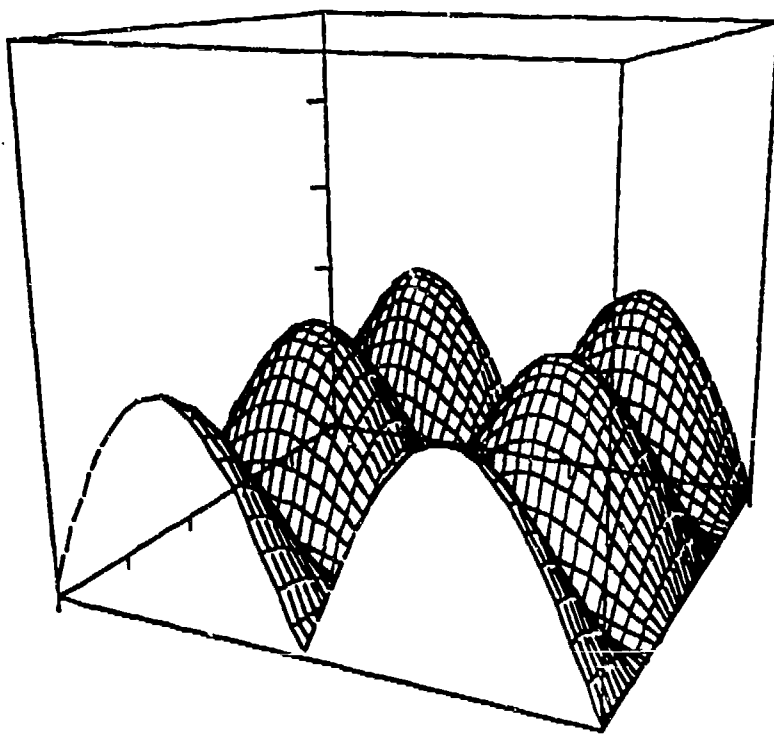


Figure 30: Three-dimensional relief map of the 212 mode at resonance (538 MHz), in the $y=y_0/2$ plane.

The double probe configurations were performed in the same way as the single probe configurations as far as the positioning of the probes was concerned. The presence of the dummy probe did however, influence the measurements. Because the reflected fields from the dummy probe were approximately 180° out of phase and were then incident on the probe being measured, a cancellation effect was taking place. This decrease in power received is displayed on the 3-dimensional relief maps by a downward slope as the distance between the probes approaches 1 cm.

The peaks and valleys for different frequencies on the graphs for both single and double probe configurations can be explained by the natural frequencies of the probes. The probes perform best when the length of the sensor was an integer multiple of a quarter wavelength of the incident wave.

As with any experiment, various sources of errors were present which may have biased some of the results. The main source of error was the instrumentation cables used in the system. The introduction of unknown errors when the cables were moved could have biased the measured values.

The IR pictures proved useful in showing the interaction between the incident EM waves and the probes. They also showed that configuration A provided for the least amount of field disturbance in the presence of the probes. It was seen, however, that the D-dot probe disturbed the field more than the B-dot probe because of its size. The large size of the D-dot probe does have the advantage that it is much sturdier and will take more abuse over a period of time and, thus, perform more consistently.

For the CUBE tests, the dependency on configuration was not as dramatic for either probe. This is because the fields being measured were no longer traveling TEM waves. Instead, the probes were measuring field distributions inside the CUBE determined by the aperture and the resonant modes of the CUBE. Inside the CUBE, the E and H components were incident on the probes from different directions and orientations. For any given operating frequency (and thus mode), the data were somewhat consistent with configuration changes. Examination of the IR pictures did reveal that the probes disturbed the field and, as before, the D-dot probe had a greater affect because of its size.

VIII. CONCLUSIONS

From the above electrical measurements and IR pictures of the response of B-dot and D-dot probes in Configurations A, B and C and rotations 0° , 90° , 180° and 270° , in free space and in a CUBE, the following conclusions are made:

When using the probes, in the free-field, they should be positioned such that the incident waves can be measured without the body of the probe affecting the measurements (configuration A). When two or more probes are used together, for example, to map a field distribution over a specified area, they should be spaced far enough apart (approximately 5 cm or more for a 10cm probe) so that coupling effects between the probes do not bias the measurements. Also, the B-dot probe should, in general, give more accurate results. Because of its size, it does not disturb the field being measured as much as the D-dot probe.

For the restricted frequency range from 1GHz to 10GHz studied in this report, the probes were used in their electrically "resonant" range of being approximately one-half wavelength from tip to base. These 10cm probes are half-wave resonant at 3GHz. Therefore, they range between three-tenths to three wavelengths in electrical length. In this restricted wavelength region, a general "rule of thumb," can be described.

For the worst case coupling (Configuration C), one probe should not be placed closer to another probe than the diameter of the sphere which would completely circumscribe either probe, i.e. the interior of the spheres which circumscribe each probe should not be allowed to intersect. This sphere that circumscribes the probe is the "sphere of influence" of the measurement.

When using the probes in an enclosed area surrounded by metal, e.g. in a cavity, the position of the probes inside the cavity can have an affect on the measurements. Again, the B-dot probe should give more accurate results because of its smaller size.

Specifically, a probe should not be placed closer to any wall of the cavity than the radius of the sphere which would completely circumscribe the probe, i.e. the interior volume of the sphere which circumscribes the probe should not be allowed to intersect any wall of the cavity.

Therefore, as many probes as desired can be placed inside a cavity to sample the interior field of the cavity, provided no circumscribing sphere of any probe intersects any other circumscribing sphere or any wall of the cavity. If these conditions are met, the measurements will not be degraded by any mutual coupling effects between the probes or between a probe and its image in the wall of the cavity.

For the 10cm B-dot and D-dot probes studied in this report, the diameters of the circumscribing spheres are approximately 10cm for both cases. Therefore, if these probes were separated by 10cm, the measurements produced by an array of such probes would be free of mutual coupling effects. The smallest volume, over which a probe could accurately sample the field in Configuration C, is the volume interior to a 10cm sphere.

Note that for the other coupling cases (Configurations A or B), the mutual coupling effects are somewhat reduced. For these cases, the above rule for the coupling distance could be relaxed somewhat, such that the circumscribing spheres could be allowed to penetrate each other up to one radius of the spheres, i.e. the interior volume of any one circumscribing sphere should not touch the surface of another probe or any wall of the cavity.

For the 10cm B-dot and D-dot probes studied in this report, this relaxed rule of distance for mutual coupling effects means that the probes could be placed as close as 5cm to each other without any significant mutual coupling effects occurring in the measurement results. The smallest volume over which a probe could accurately sample the electric or magnetic field in configurations B or C, is the interior volume of a 5cm sphere.

Note that if the probes were operated in a much higher frequency range in which they would be electrically small, the probes would appear to be effectively electrically far apart from each other and very little mutual coupling would occur; the above "rule of thumb" would not apply. Conversely, if the probes were operated in a much lower frequency range in which they would be electrically large, the probes would appear to be effectively electrically close to each other and very large mutual coupling effects would occur and dominate all measurement positions; the above "rule of thumb" would also not apply.

Also, note that surface mounted probes would be much preferred over a free field probe, since the output cable could be hidden behind the ground plane on which the probe is mounted.

The above conclusions, regarding general rules for single and double B-dot and D-dot probe measurements, can provide general guidance on correct probe measurement techniques in this restricted measurement regime of "resonant" probes to insure that accurate measurement data will be collected on Air Force equipment inside shielded enclosures when performing multiple probe tests.

REFERENCES

1. R.M. Sega and J.D. Norgard, "An Infrared Measurement Technique for the Assessment of Electromagnetic Coupling," Proceedings of the NSRE Conference, Monterey, CA, July 1985, & IEEE NS-Transactions, Vol. 32, No. 6, December 1985.
2. R.M. Sega and J.D. Norgard, "Infrared Detection of Microwave Scattering from Cylindrical Structures," Proceedings of the 1986 URSI Winter Meeting, Boulder, CO, January 1986.
3. R.M. Sega and J.D. Norgard, "Infrared Diagnostic Techniques for High-Power Microwave Technology," Proceedings of the 1986 HPM Technology Meeting, Albuquerque, NM, December, 1986.
4. R.M. Sega and J.D. Norgard, "Infrared Measurement of Scattering and Electromagnetic Penetrations through Apertures," Proceedings of the NSRE Conference, Providence, RI, July 1986, & IEEE NS-Transactions, Vol. 33, No. 6, December 1986.
5. J.D. Norgard and R.M. Sega, "Microwave Fields Determined from Thermal Patterns," Proceedings of the 1987 SPIE Symposium, Orlando, FL, May 1987.
6. R.M. Sega, D. Fredal and J.D. Norgard, "Initial Feasibility Test in an Infrared Diagnostic for High Power Microwave Applications," Proceedings of the 1987 SPIE Symposium, Orlando, FL, May 1987.
7. J.D. Norgard and R.M. Sega, "Measured Internal Coupled Electromagnetic Fields Related to Cavity and Aperture Resonance," Proceedings of the NSRE Conference, Snowmass, CO, July 1987 & IEEE NS-Transactions, Vol. 34, No. 6, December 1987.
8. R.M. Sega, J.D. Norgard and M.O. Harrison, "Infrared Comparisons of the Electromagnetic Scattering from Conducting and Dielectric Cylinders," Proceedings of the NEM Conference, San Francisco, CA, May 1988.
- 9) C.M. Butler, "The Equivalent Radius of a Narrow Conducting Strip," IEEE Transactions on Antennas and Propagation, Vol. AP-30, July 1982.
- 10) J.R. Mautz and R.F. Harrington, "Electromagnetic Transmission Through a Rectangular Aperture in a Perfectly Conducting Plane," Report AFCRL-TR-76-0056, Air Force Cambridge Research Laboratories, February 1976.

**MISSION
OF
ROME LABORATORY**

Rome Laboratory plans and executes an interdisciplinary program in research, development, test, and technology transition in support of Air Force Command, Control, Communications and Intelligence (C³I) activities for all Air Force platforms. It also executes selected acquisition programs in several areas of expertise. Technical and engineering support within areas of competence is provided to ESD Program Offices (POs) and other ESD elements to perform effective acquisition of C³I systems. In addition, Rome Laboratory's technology supports other AFSC Product Divisions, the Air Force user community, and other DOD and non-DOD agencies. Rome Laboratory maintains technical competence and research programs in areas including, but not limited to, communications, command and control, battle management, intelligence information processing, computational sciences and software producibility, wide area surveillance/sensors, signal processing, solid state sciences, photonics, electromagnetic technology, superconductivity, and electronic reliability/maintainability and testability.